Naval Research Laboratory

Washington, DC 20375-5320

An Assessment of the Biot-Stoll Model of a Poroelastic Seabed

JAMES L. BUCHANAN

Mathematics Department
United States Naval Academy

August 5, 2005

REPORT DOCUMENTATION PAGE

1. REPORT DATE *(DD-MM-YYYY)* 05-08-2005	2. REPORT TYPE Memorandum	3. DATES COVERED *(From - To)* June 2004 - June 2005

4. TITLE AND SUBTITLE

An Assessment of the Biot-Stoll Model of a Poroelastic Seabed

5a. CONTRACT NUMBER

5b. GRANT NUMBER

5c. PROGRAM ELEMENT NUMBER
62747N

6. AUTHOR(S)

James L. Buchanan*

5d. PROJECT NUMBER

5e. TASK NUMBER
UW-747-014

5f. WORK UNIT NUMBER
71-6832

7. PERFORMING ORGANIZATION NAME(S) AND ADDRESS(ES)

Naval Research Laboratory
Acoustics Division
Washington, DC 20375-5320

8. PERFORMING ORGANIZATION REPORT NUMBER

NRL/MR/7140--05-8885

9. SPONSORING / MONITORING AGENCY NAME(S) AND ADDRESS(ES)

Office of Naval Research
One Liberty Center
875 N. Randolph St.
Arlington, VA 22203-1995

10. SPONSOR / MONITOR'S ACRONYM(S)

ONR

11. SPONSOR / MONITOR'S REPORT NUMBER(S)

12. DISTRIBUTION / AVAILABILITY STATEMENT

Approved for public release; distribution is unlimited.

13. SUPPLEMENTARY NOTES

*Mathematics Department, U.S. Naval Academy, Annapolis, MD 21402-5002

14. ABSTRACT

This report evaluates the effectiveness of the Biot-Stoll model of a poroelastic seabed in predicting experimentally observed phenomena in underwater acoustics. Discussed in the report is the derivation of the model from physical principles, including more recent extensions such as the distributed pore size formulation of Turgut and Yamamoto and a more sophisticated approach to modeling intergranular effects advocated by Chotiros and Isakson. It is found that with the incorporation of these two extensions, the Biot-Stoll model is capable of producing good agreement with experimentally measured values of compressional wave speed and attenuation. It should be noted however, that there are not currently efficacious ways of measuring the new parameters introduced by these extensions other than adjusting them to wave speed and attenuation data measured over multiple decades of frequency. Also discussed in the report are the determination of the Biot-Stoll parameters, reflection and transmission at the ocean sediment surface, models for depth-varying sediment properties and some of the difficulties with, and controversies concerning, the Biot-Stoll model.

15. SUBJECT TERMS

Underwater acoustics	Bottom scattering
Poroelasticity	Biot-Stoll model

16. SECURITY CLASSIFICATION OF:			17. LIMITATION OF ABSTRACT	18. NUMBER OF PAGES	19a. NAME OF RESPONSIBLE PERSON Robert Gragg
a. REPORT Unclassified	**b. ABSTRACT** Unclassified	**c. THIS PAGE** Unclassified	UL	83	**19b. TELEPHONE NUMBER** *(include area code)* (202) 404-4816

i

An Assessment of the Biot-Stoll Model of a Poroelastic Seabed

James L. Buchanan
Mathematics Department
United States Naval Academy

May 26, 2005

Contents

1 Introduction

The purpose of this report is to assess the mathematical models currently available for predicting the acoustic behavior of a seabed at frequencies up to about $500\,\mathrm{kHz}$. For unconsolidated seabeds there are currently two rival models, the general model of a poroelastic medium due to Biot [4] and particularized by Stoll [37] to seabeds, and the model of Buckingham [11], [12], [13]. The Biot-Stoll model treats a poroelastic medium as an elastic frame with interstitial pore fluid. It has two loss mechanisms, intergranular friction and viscous friction due to the motion of the frame relative to the fluid. It depends upon thirteen parameters, which are listed in Table 1. The Buckingham model is derived from the linearized Navier-Stokes equations. Attenuation is due to grain-to-grain friction and strain hardening of the fluid between grains. It may be regarded as a causal version of the standard elastic model of the seabed in the sense that, like the elastic model, it predicts wave attenuations that are approximately linear in frequency, but unlike the elastic model, it predicts wave speeds that are logarithmically dispersive as required by the Kramers-Kronig causality relations (see Section 5.4.1).

Assessing the models requires addressing several questions

- To what extent are the predictions of the model in accord with experimental observations? In particular both models were formulated prior to Sediment Acoustics Experiment 1999 (SAX99) [41], [33] which is to date the most comprehensive attempt to measure such observables as wave speeds and attenuations for a sediment with known parameters.

- Are the underlying assumptions used in deriving the models appropriate for an unconsolidated sediment? For instance does an aggregation of uncemented sand grains constitute a Hookean elastic frame in the sense assumed by the Biot model? To the extent that this is not the case what modifications are necessary?

- Is the Biot model unnecessarily complicated? The conventional model Biot-Stoll model depends upon thirteen input parameters, some of which are not easy to measure. Are the viscous losses predicted by the Biot

model due to the relative motion of the fluid and frame important for unconsolidated seabeds? If not might the simpler Buckingham model which requires only five inputs suffice?

Let us begin by illustrating the different predictions the two models make in regards to wave speeds and attenuations. Figures 1 and 2 illustrate the differences. The measured values of compressional wave speed and attenuation were taken from Williams *et al.* [44], Figure 6. They are a compilation of measurements made during Sediment Acoustics Experiment 1999 (SAX99) [41], [33]. The parameters used in the Biot-Stoll model to produce the prediction labelled "Best in range fit" in the Figures are given in Table 1, Column 4, and are also from [44]. These were chosen to give the best fit to the data using parameter values that were within the range estimates[1] in Table 1, Column 3. The authors noted that better agreement with the two measurements of compressional wave speed below $1\,\mathrm{kHz}$ resulted from changing the parameters porosity, tortuosity and permeability[2] to $\beta = 41.5, \alpha = 1.12, k = 5 \times 10^{-11}$, all of which lie outside of the estimated ranges. These Biot predictions are labelled "Best fit". As indicated in Figure 1 the Biot model predicts that compressional wave speed will be much more dispersive with respect to frequency than the Buckingham model and is in better accord with the measured wave speeds. On the other hand Figure 2 shows that the Biot model underestimates the compressional wave attenuation at frequencies above $100\,\mathrm{kHz}$ while the Buckingham model is in good agreement at all frequencies. To date no one has offered a means to correct the Buckingham model's failure to predict the velocity dispersion observed in the SAX99 exercise and in other experiments. There have recently been successes in improving the Biot model's predictions, however, and so the report will focus on this model.

2 Derivation of the equations of the Biot-Stoll model

Biot developed his model for a poroelastic medium in a series of papers [3], [6], [7], [5], [4], [8] written over the course of more than twenty years. It is a general model which has been applied to areas of science and engineering as diverse as seabeds, soundproofing and ultrasound propagation through bone.

2.1 Constitutive equations

Biot's notation changed over the course of the years. In deriving the constitutive equation and equations of motion we follow Biot [4] and Stoll [37] since the notation in these articles is the most commonly used in seabed acoustics. The medium is regarded as an elastic frame with an interstitial pore fluid. Two

---

[1] The authors' estimates of the parameter ranges are selective; they chose to disregard some measurements of the parameters that they deemed unreliable.

[2] Unless othrwise indicated, the units for physical parameters are meters-kilogram-seconds.
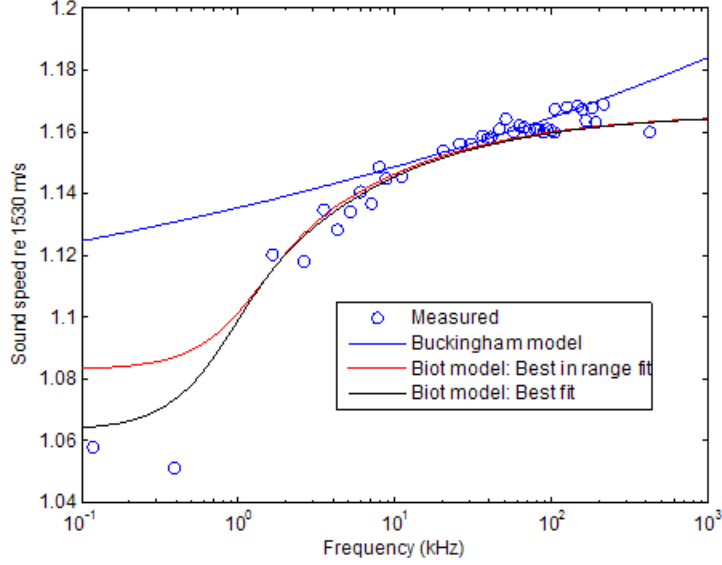
Figure 1: SAX99 measurements of compressional wave speed. The Buckingham model predictions were computed from the best fit parameters in Table 1 assuming $c_p = 1771\,\mathrm{m\,/\,s}$ at $38\,\mathrm{kHz}$, $c_s = 129\,\mathrm{m\,/\,s}$, $\alpha_s = 30$ dB/m at $1\,\mathrm{kHz}$.

Symbol	Parameter	Range	Best fit
ρ_f	Density of the pore fluid	$[1020, 1023]$	$1023\,\mathrm{kg\,/\,m^3}$
ρ_r	Density of sediment grains	$[2664, 2716]$	$2690\,\mathrm{kg\,/\,m^3}$
$K_b = \mathrm{Re}\,K_b^*$	Real frame bulk modulus		$4.36 \times 10^7\,\mathrm{Pa}$
$\mathrm{Im}\,K_b^*$	Imag frame bulk modulus		$-2.08 \times 10^6\,\mathrm{Pa}$
$\mu = \mathrm{Re}\,\mu^*$	Real frame shear modulus	$[1.7, 4.3] \times 10^7$	$2.92 \times 10^7\,\mathrm{Pa}$
$\mathrm{Im}\,\mu^*$	Imag frame shear modulus	$-[1.3, 2.6] \times 10^7$	$-1.8 \times 10^6\,\mathrm{Pa}$
K_f	Fluid bulk modulus	$[2.37, 2.42] \times 10^9$	$2.395 \times 10^9\,\mathrm{Pa}$
K_r	Grain bulk modulus	$[3.2, 4.9] \times 10^{10}$	$3.2 \times 10^{10}\,\mathrm{Pa}$
β	Porosity	$[0.363, 0.394]$	0.385
η	Viscosity of pore fluid	$[0.95, 1.15] \times 10^{-3}$	$1.05 \times 10^{-3}\,\mathrm{kg\,/\,m \cdot s}$
k	Permeability	$[2.1, 4.5] \times 10^{-11}$	$2.5 \times 10^{-11}\,\mathrm{m^2}$
α	Tortuosity	$[1.19, 1.57]$	1.35
a	Pore size parameter		$2.65 \times 10^{-5}\,\mathrm{m}$

Table 1: Parameter ranges for the Biot-Stoll model measured in SAX99. The pore size parameter was caluculated from other parameters. The real and imaginary parts of the frame bulk modulus were taken from the literature.
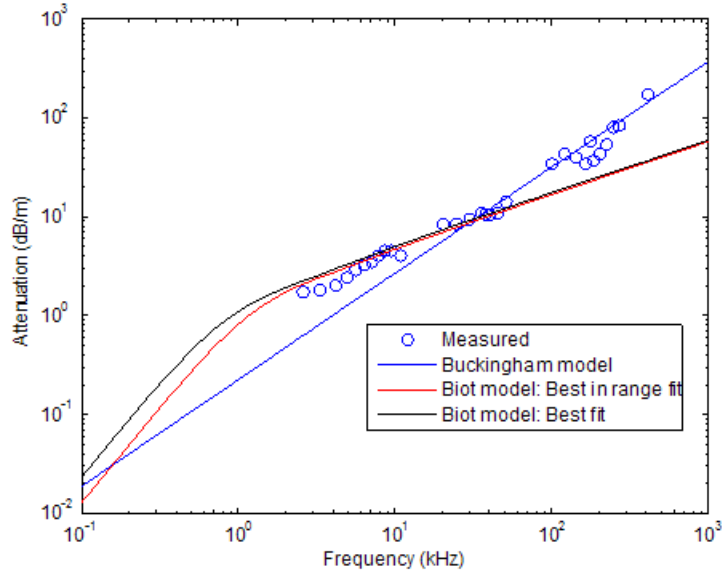
Figure 2: SAX99 measurements of compressional wave attenuation. The Buckingham model predictions were computed from the best fit parameters in Table 1 assuming $c_p = 1771 \, \mathrm{m \, / \, s}$ at $38 \, \mathrm{kHz}$, $c_s = 129 \, \mathrm{m \, / \, s}$, $\alpha_s = 30$ dB/m at $1 \, \mathrm{kHz}$.

displacement vectors $\boldsymbol{u}(x,y,z,t) = [u_x(x,y,z,t), u_y(x,y,z,t), u_z(x,y,z,t)]$ and $\boldsymbol{U}(x,y,z,t) = [U_x(x,y,z,t), U_y(x,y,z,t), U_z(x,y,z,t)]$ track the macroscopic motion of the frame and fluid respectively while the divergences $e = \nabla \cdot \boldsymbol{u}$ and $\epsilon = \nabla \cdot \boldsymbol{U}$ give the frame and fluid dilatations. For an isotropic elastic body the strain energy is a function

$$W = W(I_1, I_2, I_3)$$

of the three elastic invariants (see Love [29])

$$I_1 = e_{xx} + e_{yy} + e_{zz} = e$$

$$I_2 = e_{yy}e_{zz} + e_{xx}e_{zz} + e_{xx}e_{yy} - \frac{1}{4}\left(e_{yz}^2 + e_{xz}^2 + e_{xy}^2\right)$$

$$I_3 = e_{xx}e_{yy}e_{zz} + \frac{1}{4}\left(e_{yz}e_{xz}e_{xy} - e_{xx}e_{yz}^2 - e_{yy}e_{xz}^2 - e_{zz}e_{xy}^2\right).$$

where the strains are related to the displacements by

$$e_{xx} = \frac{\partial u_x}{\partial x}, e_{yy} = \frac{\partial u_y}{\partial y}, e_{zz} = \frac{\partial u_z}{\partial z} \tag{1}$$

$$e_{xy} = \frac{\partial u_x}{\partial y} + \frac{\partial u_y}{\partial x}, e_{xz} = \frac{\partial u_x}{\partial z} + \frac{\partial u_z}{\partial x}, e_{yz} = \frac{\partial u_y}{\partial z} + \frac{\partial u_z}{\partial y}.$$

For a poroelastic medium a strain energy function of the form

$$W = W(I_1, I_2, I_3, \zeta)$$

is posited. The additional quantity is the *increment of fluid content*

$$\zeta = \beta(e - \epsilon) \tag{2}$$

where β denotes the porosity of the medium. For small displacements a strain energy function can be taken to be a linear function of the quadratic terms only

$$W = W(I_1, I_2, \zeta) = \frac{H}{2}e^2 - 2\mu I_2 - Ce\zeta + \frac{M}{2}\zeta^2.$$

The choice of symbols for the coefficients is made simply to arrive at the form of the constitutive equations given in [4]. The six distinct aggregate stresses on an element of the medium are denoted by

$$\tau_{xx}, \tau_{xy}, \tau_{xz}, \tau_{yy}, \tau_{yz}, \tau_{zz}.$$

The constitutive equations are then found by differentiation $\tau_{xx} = \frac{\partial W}{\partial e_{xx}}, \tau_{xy} = \frac{\partial W}{\partial e_{xy}} \ldots, p_f = \frac{\partial W}{\partial \zeta}$, where p_f is the pore fluid pressure, to be

$$\tau_{xx} = He - 2\mu\left(e_{yy} + e_{zz}\right) - C\zeta \tag{3}$$
$$\tau_{yy} = He - 2\mu\left(e_{xx} + e_{zz}\right) - C\zeta$$
$$\tau_{zz} = He - 2\mu\left(e_{xx} + e_{yy}\right) - C\zeta$$
$$\tau_{xy} = \mu e_{xy}, \ \tau_{xz} = \mu e_{xz}, \ \tau_{yz} = \mu e_{yz}$$
$$p_f = M\zeta - Ce.$$

6

From these equations the modulus μ is seen to be the Lamé shear coefficient. In the absence of the two fluid coefficients C and M the first four equations become those of an elastic solid with the modulus H becoming the Lamé compressional coefficient.

In order to relate the moduli H, C and M to standard quantities in elastic and fluid media, Stoll followed Biot and Willis [5] in considering two thought experiments:

- The *jacketed test* (Figure 3) in which a saturated sample of the porous medium is placed in a flexible, impervious jacket and a constant external pressure p' is applied. Fluid is allowed to drain from the sack in order to keep the fluid pressure constant, whence it may be normalized to $p_f = 0$. In this case the frame will exert an equilibrating counter pressure $K_b e = -p'$ where K_b is the frame's bulk modulus.

- The *unjacketed test* (Figure 4) in which a sample of the medium is immersed in fluid and a uniform pressure p' is applied to the surface of the fluid. In this case $p_f = p'$ and the counteracting pressures are $K_r e = K_f \epsilon = -p'$ and $K_{fr} \zeta = p'$, where K_r is the bulk modulus of the frame material, K_f is the bulk modulus of the fluid, and K_{fr} is another modulus.

In either test

$$\tau_{xx} = \tau_{yy} = \tau_{zz} = -p'$$
$$\tau_{xy} = \tau_{xz} = \tau_{yz} = 0.$$

Upon substituting the first equation into the first three equations of (3) and then adding the equations together we obtain

$$-p' = He - 4/3\mu e - C\zeta. \tag{4}$$

For the jacketed test we then have from (4)

$$K_b = H - 4/3\mu - C\zeta/e.$$

By setting $p_f = 0$ in the last equation in (3) we obtain

$$\zeta/e = C/M$$

whence

$$K_b = H - 4/3\mu - C^2/M. \tag{5}$$

For the unjacketed test we have from (4)

$$K_r = H - 4/3\mu + CK_r/K_{fr}. \tag{6}$$

Also for the unjacketed test we have from the last equation in (3)

$$1 = M/K_{fr} + C/K_r \tag{7}$$

7

Solving (5),(6) and (7) for H, C and M gives

$$H = K_b + \frac{4}{3}\mu + \frac{(K_r - K_b)^2}{D - K_b} \tag{8}$$

$$C = \frac{K_r(K_r - K_b)}{D - K_b}$$

$$M = \frac{K_r^2}{D - K_b}$$

where

$$D = K_r(1 + K_r/K_{fr}). \tag{9}$$

If the sample undergoes no change in porosity during the unjacketed test then

$$\zeta = \beta(e - \epsilon) = \beta\left(-\frac{p'}{K_r} + \frac{p'}{K_f}\right)$$

and thus K_{fr} is related to the bulk modulus K_f of the pore fluid by

$$\frac{1}{K_{fr}} = \beta\left(\frac{1}{K_f} - \frac{1}{K_r}\right) \tag{10}$$

in which case

$$D = K_r(1 + \beta(K_r/K_f - 1)). \tag{11}$$

Observe that the first two terms of $(8)_1$ are the compressional Lamé coefficient of an elastic solid. The last term then represents a correction for the presence of the pore space. It goes to zero as $\beta \to 0$ and $K_r \to K_b$.

2.2 Equations of motion

In [4] Biot derived equations of motion for a poroelastic medium from Lagrange's equations

$$\frac{\partial \tau_{xx}}{\partial x} + \frac{\partial \tau_{xy}}{\partial y} + \frac{\partial \tau_{xz}}{\partial z} = \frac{\partial}{\partial t}\left(\frac{\partial T}{\partial \dot{u}_x}\right) \tag{12}$$

$$\frac{\partial \tau_{xy}}{\partial x} + \frac{\partial \tau_{yy}}{\partial y} + \frac{\partial \tau_{yz}}{\partial z} = \frac{\partial}{\partial t}\left(\frac{\partial T}{\partial \dot{u}_y}\right)$$

$$\frac{\partial \tau_{xz}}{\partial x} + \frac{\partial \tau_{yz}}{\partial y} + \frac{\partial \tau_{zz}}{\partial z} = \frac{\partial}{\partial t}\left(\frac{\partial T}{\partial \dot{u}_z}\right)$$

$$\frac{\partial p_f}{\partial x} = \frac{\partial}{\partial t}\left(\frac{\partial T}{\partial \dot{w}_x}\right) + \frac{\partial D}{\partial \dot{w}_x}$$

$$\frac{\partial p_f}{\partial y} = \frac{\partial}{\partial t}\left(\frac{\partial T}{\partial \dot{w}_y}\right) + \frac{\partial D}{\partial \dot{w}_y}$$

$$\frac{\partial p_f}{\partial z} = \frac{\partial}{\partial t}\left(\frac{\partial T}{\partial \dot{w}_z}\right) + \frac{\partial D}{\partial \dot{w}_z}.$$
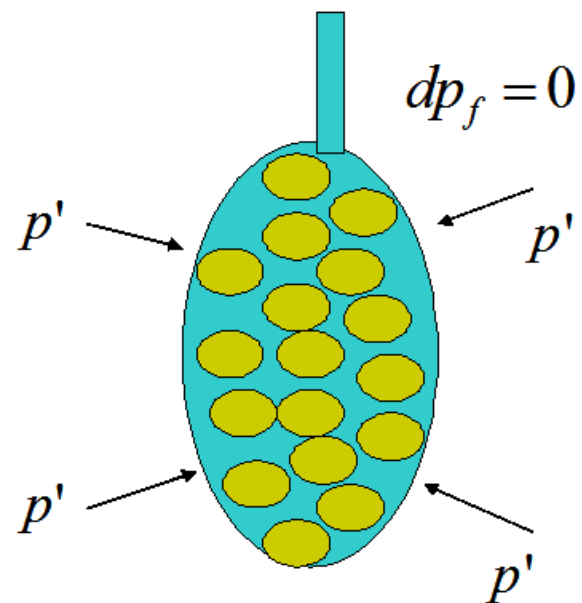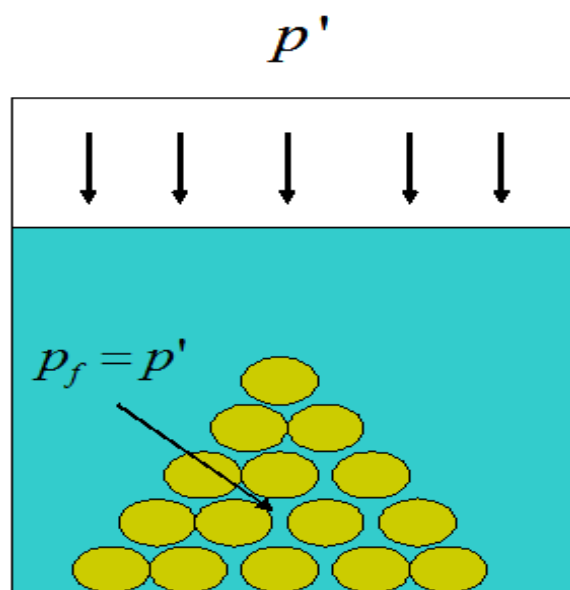
Figure 3: Jacketed test.

Figure 4: Unjacketed test.

with the kinetic energy function

$$T = \tag{13}$$
$$\frac{1}{2}\left[\rho\left(\dot{u}_x^2 + \dot{u}_y^2 + \dot{u}_z^2\right) - 2\rho_f\left(\dot{u}_x\dot{w}_x + \dot{u}_y\dot{w}_y + \dot{u}_z\dot{w}_z\right) + m\left(\dot{w}_x^2 + \dot{w}_y^2 + \dot{w}_z^2\right)\right]$$

and the Rayleigh dissipation function

$$D = \frac{1}{2}d\left[\dot{w}_x^2 + \dot{w}_y^2 + \dot{w}_z^2\right].$$

Here $\rho = (1-\beta)\rho_r + \beta\rho_f$ is the aggregate density of the medium, ρ_r is the density of the frame material, ρ_f is the density of the pore fluid, and m and d are mass and dissipation parameters which will be discussed shortly. The vector

$$\boldsymbol{w} = \beta(\boldsymbol{u} - \boldsymbol{U})$$

measures the relative displacement of the frame and fluid. The dots over the components of $\boldsymbol{u}$ and $\boldsymbol{w}$ denote partial derivatives with respect to time. When the expressions for T and D are substituted into (12) the following equations of motion result

$$\mu\nabla^2\boldsymbol{u} + \nabla[(H - \mu)e - C\zeta] = \frac{\partial^2}{\partial t^2}(\rho\boldsymbol{u} - \rho_f\boldsymbol{w}) \tag{14}$$

$$\nabla[Ce - M\zeta] = \frac{\partial^2}{\partial t^2}(\rho_f\boldsymbol{u} - m\boldsymbol{w}) - d\frac{\partial}{\partial t}\boldsymbol{w}.$$

For uniform pore size and a flow parallel to the pore direction, the mass parameter m would be ρ_f/β, so that in $(14)_2$ $\rho_f\boldsymbol{u} - m\boldsymbol{w} = \rho_f\boldsymbol{U}$, but given that not all of the fluid will flow in the direction of the macroscopic pressure gradient due to the tortuosity of the pore space, Stoll [37] takes the parameter m to be

$$m = \frac{\alpha\rho_f}{\beta}, \alpha \geq 1$$

where α is referred to as the *tortuosity*[3]. Stoll states that for pores with all possible orientations the value of α would be 3, but he gives no explanation or citation.

Finally note that the dissipation term in $(14)_2$ has the dimensions of a pressure gradient. According to Darcy's law for steady laminar (Poiseuille) flow through a porous medium the average seepage velocity $\langle V \rangle$ due to a pressure gradient $\frac{\partial p}{\partial x}$ is

$$\langle V \rangle = -\frac{k}{\beta\eta}\frac{\partial p}{\partial x}, \tag{15}$$

where β and k are the porosity and permeability of the medium. Identifying $-\beta\langle V \rangle$ with $\frac{\partial}{\partial t}\boldsymbol{w}$ in $(14)_2$, suggests that the parameter d should be

$$d = \frac{\eta}{k}.$$

This is the case for only Poiseuille flow, however. The modification required for oscillatory motion is discussed in the next section.

---

[3]It is also referred to as the structure factor or constant or the virtual mass coefficient.

2.3 The general form of the dissipation parameter

To find the form of the dissipation parameter d in $(14)_2$ we need to calculate the ratio of the force per unit volume exerted on the pore walls to the average velocity of the fluid flowing through the pore space. Biot [7] solved the problem of fluid motion in a duct for two cases that he regarded as opposing extremes, a cylindrical duct and a duct between two parallel plates, the latter approximately representing the case of flat ovaloid pores. Consider a flow in the x-direction for each case. For a cylinder of radius a with spatial coordinates (x, r, θ) considerations of symmetry dictate that the velocity of the flow V will depend only on r and time t and the stress τ on the wall of the cylinder only on t. The dissipation parameter d will take the form

$$d = \frac{\frac{2\pi a \tau \Delta x}{\pi a^2 \Delta x}}{\beta \langle V \rangle} = \frac{2\tau}{\beta a \langle V \rangle} \tag{16}$$

where $\pi a^2 \Delta x$ is the volume of an arbitrary element of the cylindrical duct and $\langle V \rangle$ denotes the average seepage velocity. On the other hand for two plates of separation $2a_1$ with spatial coordinates $(x, y, z), -a_1 \le y \le a_1$ considerations of symmetry dictate that the stress τ is the same on the top and bottom plates whence for an arbitrary element of the duct

$$d = \frac{\frac{2\tau \Delta x \Delta z}{\Delta x \Delta y \Delta z}}{\beta \langle V \rangle} = \frac{\tau}{\beta a_1 \langle V \rangle}. \tag{17}$$

The position of the fluid $U(r, t)$ is governed by the linearized Navier-Stokes equation

$$\rho_f \frac{\partial^2 U}{\partial t^2} = -\frac{\partial p}{\partial x} + \eta \nabla^2 \left(\frac{\partial U}{\partial t} \right).$$

Here η is fluid viscosity and the pressure gradient $\frac{\partial p}{\partial x}$ is assumed to depend upon time, but to be independent of the spatial coordinates. The position $u(t)$ of the walls of the duct is also assumed to be independent of x. The relative velocity $V(r, t) = \frac{\partial}{\partial t} (U(r, t) - u(t))$ then satisfies

$$\eta \nabla^2 V - \rho_f \frac{\partial V}{\partial t} = -\rho_f X := \frac{\partial p}{\partial x} + \rho_f \frac{d^2 u}{dt^2}. \tag{18}$$

Steady, laminar flow in which the inertial terms $\frac{\partial V}{\partial t}, \frac{d^2 u}{dt^2}$ in (18) are neglected is termed *Poiseuille flow*. For the case of cylindrical ducts the solution of the differential equation

$$\eta \left(\frac{d^2 V}{dr^2} + \frac{1}{r} \frac{dV}{dr} \right) = \frac{\partial p}{\partial x}, V(a) = 0$$

is

$$V(r) = \frac{1}{4\eta} \frac{\partial p}{\partial x} \left(r^2 - a^2 \right)$$

and the average velocity is given by

$$\langle V \rangle = \frac{1}{4\eta}\frac{\partial p}{\partial x}\frac{1}{\pi a^2}\int_0^a\int_0^{2\pi}\left(r^2 - a^2\right)rd\theta dr = -\frac{a^2}{8\eta}\frac{\partial p}{\partial x}. \tag{19}$$

Comparison of (19) with Darcy's law (15) gives

$$k = \frac{\beta a^2}{8} \tag{20}$$

for the permeability of a cylindrical duct. The stress at the wall of the duct is

$$\tau = -\eta V'(a) = -\frac{a}{2}\frac{\partial p}{\partial x} \tag{21}$$

and thus from (16)

$$d = \frac{2\tau}{\beta a\langle V\rangle} = \frac{8\eta}{\beta a^2} = \frac{\eta}{k}.$$

For the case of Poiseuille flow in a pore duct between parallel plates equation (18) gives

$$\eta\frac{d^2V}{dy^2} = \frac{\partial p}{\partial x}, V(\pm a_1) = 0$$

which has solution

$$V(y) = \frac{1}{2\eta}\frac{\partial p}{\partial x}\left(y^2 - a_1^2\right).$$

The average velocity is then

$$\langle V\rangle = \frac{1}{2\eta}\frac{\partial p}{\partial x}\frac{1}{2a_1}\int_{-a_1}^{a_1}\left(y^2 - a_1^2\right)dy = -\frac{1}{3\eta}\frac{\partial p}{\partial x}a_1^2.$$

From Darcy's law (15) it follows that

$$k = \frac{\beta a_1^2}{3}. \tag{22}$$

The stress on the wall is

$$\tau = -\eta V'(a_1) = -a_1\frac{\partial p}{\partial x}$$

and thus from (17)

$$d = \frac{\tau}{\beta a_1\langle V\rangle} = \frac{3\eta}{\beta a_1^2} = \frac{\eta}{k}.$$

If the duct is assumed to be undergoing time-harmonic oscillations $V(x,y,z,t) = V(x,y,z)e^{i\omega t}, \frac{\partial p}{\partial x}(t) = \frac{\partial p}{\partial x}e^{i\omega t}, u(t) = ue^{i\omega t} \Rightarrow X(t) = \left(-\frac{1}{\rho_f}\frac{\partial p}{\partial x} + \omega^2 u\right)e^{i\omega t} \equiv Xe^{i\omega t}$, then (18) becomes

$$\eta\nabla^2 V - i\omega\rho_f V = -\rho_f X. \tag{23}$$

12

Note that $\omega = 0$ corresponds to Poiseuille flow. For the case of a cylindrical duct (23) has solution

$$V(r) = \frac{X}{i\omega}\left(1 - \frac{J_0\left(i^{3/2}\kappa r/a\right)}{J_0\left(i^{3/2}\kappa\right)}\right)$$

where

$$\kappa = a\sqrt{\frac{\omega\rho_f}{\eta}} \equiv \chi(\omega)a. \tag{24}$$

The average velocity is then

$$\langle V \rangle = \frac{2}{a^2}\int_0^a V(r)r\,dr = \frac{X}{i\omega}\left(1 + \frac{2\sqrt{i}J_1\left(i^{3/2}\kappa\right)}{\kappa J_0\left(i^{3/2}\kappa\right)}\right) = \frac{X}{i\omega}\left(1 + \frac{2i}{\kappa}T(\kappa)\right) \tag{25}$$

where

$$T(\kappa) = \frac{J_1(i^{3/2}\kappa)}{\sqrt{i}J_0(i^{3/2}\kappa)}.$$

The stress at the wall is

$$\tau = -\eta V'(a) = -\eta\frac{X}{i\omega}\frac{i^{3/2}\kappa J_1\left(i^{3/2}\kappa\right)}{aJ_0\left(i^{3/2}\kappa\right)} = \frac{\eta\kappa X}{i\omega a}T(\kappa) \tag{26}$$

and thus

$$d = \frac{2\tau}{\beta a\langle V\rangle} = \frac{8\eta}{\beta a^2}F(\kappa) = \frac{\eta}{k}F(\kappa)$$

where

$$F(\kappa) = \frac{1}{4}\frac{\kappa T(\kappa)}{1 + \frac{2i}{\kappa}T(\kappa)}.$$

Figure 5 shows the function $F(\kappa)$. As can be seen $F(\kappa) \to 1$ as $\kappa \to 0$, thus giving $d = \eta/k$ for Poiseuille flow in the low frequency limit.

For the case of flow between two plates of separation $2a_1$ we obtain

$$d = \frac{\eta}{k}F_1(\kappa_1)$$

where

$$\kappa_1 = \chi(\omega)a_1, F_1(\kappa) = \frac{1}{3}\frac{\sqrt{i}\kappa\tanh\sqrt{i}\kappa}{1 + \frac{i}{\kappa}\tanh\sqrt{i}\kappa}.$$

Observing that the curves $\operatorname{Re}F_1(\kappa_1)$ and $\operatorname{Im}F_1(\kappa_1)$ were almost indistinguishable from the curves $\operatorname{Re}F(\kappa)$ and $\operatorname{Im}F(\kappa)$ with $a = 4a_1/3$ in (24), Biot conjectured that it might be possible to compensate for the deviation from Poiseuille flow with increasing frequency by using the complex-valued dynamic viscosity $\eta F(\kappa)$ with the *pore size parameter* a in (24) being chosen appropriately for the dimensions and geometry of the pores. He did not give much guidance as to how to measure the pore size parameter other than to suggest is might be ascertainable from experimental data on dispersion of wave speed and attenuation
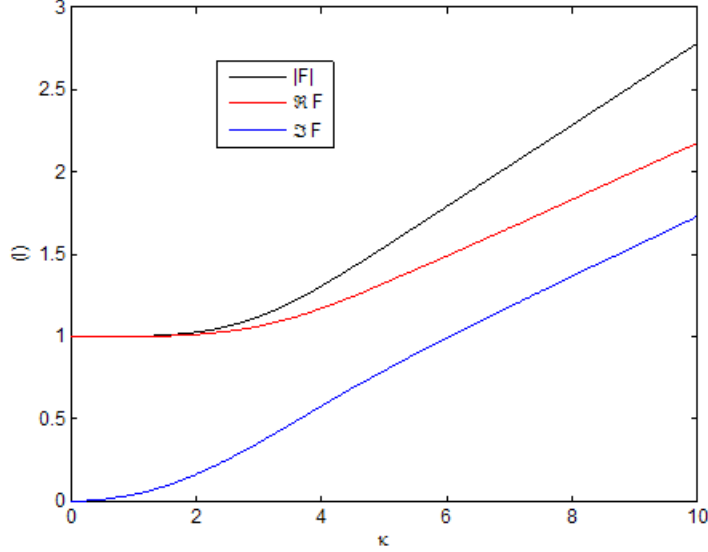
13

Figure 5: Biot's function $F(\kappa)$.

with respect to frequency. The dissipation parameter d in $(14)_2$, then is given by

$$d = \frac{\eta}{k} F\left(\chi(\omega)a\right)$$

for any pore shape for which the pore size parameter is ascertainable. When the time-harmonic factor is $e^{-i\omega t}$, rather than $e^{i\omega t}$, then d is replaced by its complex conjugate $\bar{d}$. Figure 6 shows the effect that the presence of the factor $F(\kappa)$ has on the Biot model's prediction for compressional wave speed and attenuation when the parameters of Table 1, Column 4 are used.

2.4 Incorporation of viscoelastic intergranular effects

The only loss mechanism considered thus far is viscous loss due to the relative motion of the frame and the pore fluid. Clearly other loss mechanisms such as intergranular friction may be of significance. Following the suggestion of Stoll [37] (see also [39]) most authors have attempted to incorporate such losses by giving the moduli μ and K_b small imaginary parts which are independent of frequency (see Section 3.5). However, as noted by Turgut [42], this model is not consistent with the Kramers-Kronig causality relations. Moreover recent work by Chotiros and Isakson [17] suggests that a more sophisticated approach to modelling microscopic granular effects may rectify the Biot models poor predictions for compressional wave attenuation at high frequencies that is illustrated in Figure 2.
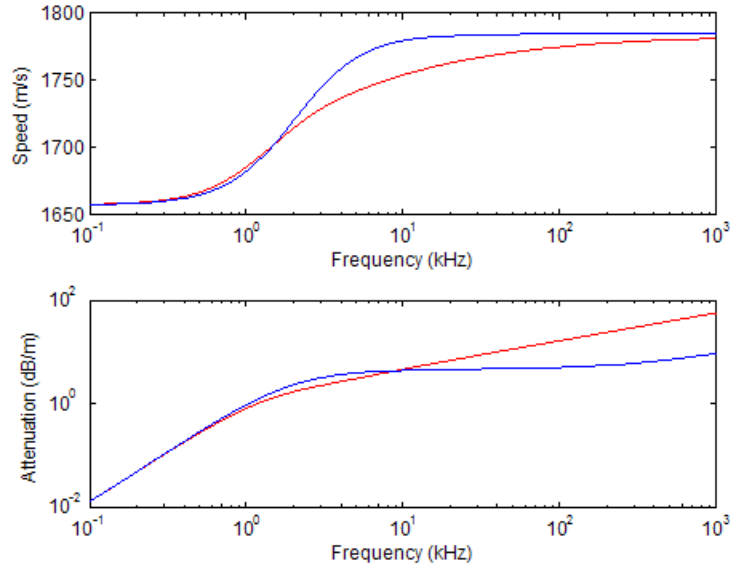
14

Figure 6: The blue line is the Biot model prediction when $d = \eta F(\kappa)/k$. The red line is the prediction when $d = \eta/k$. The upper graph is compressional wave speed and the lower graph is compressional wave attenuation. The Biot-Stoll parameters are the best fit parameters of Table 1.
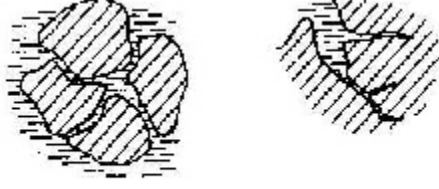
FIG. 4. Illustration of actual grain and fluid gap configurations.

Figure 7: From [8].

In [4] Biot gave the general form

$$H^* = \frac{4}{3}\mu^* + \frac{\kappa^* + \gamma - \delta}{\kappa^*(\gamma + \delta) - \delta^2}$$

$$M^* = \frac{1}{\gamma + \delta - \delta^2/\kappa^*}$$

$$C^* = \frac{1 - \delta/\kappa^*}{\gamma + \delta - \delta^2/\kappa^*}.$$

Algebraically these equations are equations (8) rendered in terms of the compressibilities

$$\kappa^* = K_b^{-1}, \delta = K_r^{-1}, c = K_f^{-1}, \gamma = \beta\,(c - \delta)\,,$$

however Biot suggests that these moduli be regarded as operators calculated from the operators κ^* and μ^* which are chosen appropriately for the phenomenon to be modelled. We will discuss three choices of these operators which are relevant to the work of Chotiros and Isakson.

For fluid filled cracks and gaps (Figure 7) Biot [8], assuming that the normal pressure P on the gap and the change in gap width Δh are related by $P = \bar{Z}\Delta h$, arrives at the formula (Figure 8)

$$\kappa^* = \kappa_0 + \frac{1}{1/\kappa_1 + \bar{\bar{Z}}}. \tag{27}$$

For a fluid-filled gap Biot finds that pore fluid pressure satisfies the diffusion equation

$$\frac{\partial^2 p_f}{\partial x^2} = \frac{12\eta c}{h^2}\frac{\partial p_f}{\partial t}$$

where η is viscosity and h is the width of the gap (Figure 9). Thus, assuming $p_f(0,t) = p_f(D,t) = 0, p_f(x,0) = const,$

$$p_f = \sum_{n=1}^{\infty} B_n \exp\left(-\frac{12\eta c}{h^2}\left(\frac{2n-1}{D}\pi\right)^2 t\right)\sin\left(\frac{2n-1}{D}\pi x\right).$$
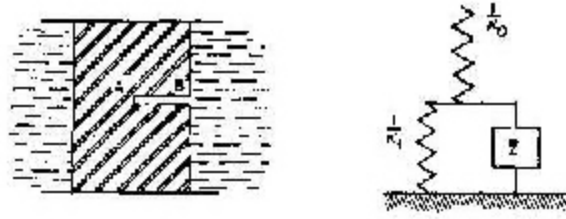
16

Fig. 7. Fluid-saturated crack AB in a solid, and its
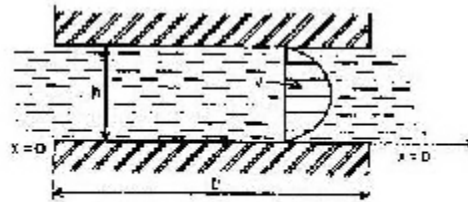equivalent block diagram.

Figure 8: From [8].

Fig. 5. Simplified model for a compressible fluid gap
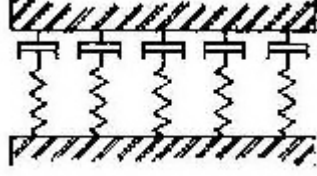between solid boundaries.

Figure 9: From [8]

FIG. 6. Maxwell elements in parallel equivalent to the fluid gap of Fig. 5.

Figure 10: From [8].

This suggested to Biot that a fluid-filled gap should be modelled as a series of Maxwell elements in parallel (Figure 10), giving

$$\bar{Z} = \sum_{n=1}^{\infty} \frac{a_n}{p + r_n}$$

where p is in general the time-derivative operator d/dt and for the specific case of time-harmonic oscillations $p = -i\omega$ and the relaxation frequencies are

$$r_n = \frac{12\eta c}{h^2}\left(\frac{2n-1}{D}\pi\right)^2.$$

Thus Biot's jacketed compressibility operator for a fluid filled crack is

$$\kappa^* = \kappa_0 + \frac{1}{1/\kappa_1 - \sum_{n=1}^{\infty}\frac{i\omega a_n}{r_n - i\omega}} \tag{28}$$

in the time-harmonic case.

Biot used the following general form for the shear modulus

$$\mu^* = \int_0^{\infty} \frac{p}{p+r}\mu(r)dr + \mu_0 + \mu_1 p.$$

For solid dissipation due to shear Biot [8] suggests the representation

$$\mu^* = \mu_0 + a(-i\omega)^s, 0 < s < 1 \tag{29}$$

which follows from assuming the relaxation spectrum

$$\mu(r) = \frac{a}{\pi}r^{s-1}\sin s\pi.$$

Finally Chotiros and Isakson [17] suggest that the presence of air bubbles in the pore space might reduce the effective fluid bulk modulus (see Section 3.3) and thereby explain the lower than predicted wave speeds below $1\,\text{kHz}$ for the SAX99 sediment that are shown in Figure 1 without assuming a higher than measured porosity. In Biot [8] posits that the presence of air bubbles in the

18

Fig. 8. Spring, mass, and dashpot model representing a fluid containing bubbles.
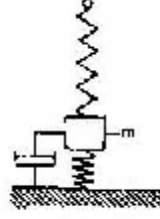
Figure 11: From [8]

pore fluid can be modelled by assuming the fluid compressibility is given by the operator (Figure 11)

$$c^* = c_0 + \frac{1}{k_a - m_a\omega^2 - ib_a\omega}. \tag{30}$$

Biot points out that if the damping constant b_a is small relative to the spring constant k_a, then there will be a resonant frequency.

2.5 Extensions and continuations of Biot's formulation

Biot recognized that his analysis assumed that the pore size distribution is narrow and that some generalization would be required for a material in which pore sizes were more widely distributed. In this section we present two subsequent extensions of Biot's formulation, the formula for the pore size parameter developed by Johnson, Koplik and Dashen [25] and the generalization of the viscosity correction factor F of Yamamoto and Turgut [45]. In this section we also describe the work of Chotiros and Isakson [17] on intergranular viscoelastic mechanisms, which represents a continuation of the work described in Section 2.4.

2.5.1 The pore size parameter for distributed pore sizes

Johnson, Koplik and Dashen [25] argue that for pores represented by non-intersecting canted cylindrical tubes of radius R

$$\frac{8\alpha_\infty k_0}{\beta R^2} = 1$$

where α_∞ is the limit of tortuosity as frequency goes to infinity and k_0 is the limit of permeability as frequency goes to zero (in their formulation α and k are frequency dependent) and offer the heuristic generalization

$$\frac{8\alpha_\infty k_0}{\beta\Lambda^2} = \varsigma \tag{31}$$

19

where $\varsigma \approx 1$ and Λ is defined by

$$\frac{2}{\Lambda} = \frac{\int_{S_p} |\boldsymbol{u}_p|^2 \, dA}{\int_{V_p} |\boldsymbol{u}_p| \, dV} \tag{32}$$

where $\boldsymbol{u}_p$ is the microscopic potential flow field, S_p is the pore-grain surface and V_p is the pore space volume. For cylindrical pores the flow field is constant in which case (32) gives $\Lambda = R$, the pore radius. Upon conducting simulations upon cubical lattices in which the pore radii were distributed according to various probability distributions they concluded that the approximation $\varsigma \approx 1$ "may be violated by a factor of 2 but not apparently by a factor of 10." If we take $\varsigma = 1$ and identify Λ with the pore size parameter, and α and k in the Biot-Stoll parameter set with α_∞ and k_0 (see below) then we arrive at the formula

$$a = \sqrt{\frac{8\alpha k}{\beta}} \tag{33}$$

for the pore size parameter for cylindrical ducts of varying radii. For flat pores the 8 is replaced by 3. While the reasoning is ad hoc, the formula has found favor. It was used to determine pore size for seabed for SAX99 by [44] (see Table 1). It is also used in the application of the Biot model to cancellous bone [20].

As mentioned above [25] assume that permeability and tortuosity are dynamic. An alternative formulation of Biot's equations due to Hovem and Ingram [24] gives a dynamic permeability and tortuosity. In $(14)_2$ take $m = \alpha_\infty \rho_f / \beta$, $d = \eta \overline{F}/k_0 = \eta (F_r - iF_i)/k_0$ and assume time-harmonic motion $e(x, y, z, t) = e(x, y, z)e^{-i\omega t}, \ldots$. The result is

$$\nabla[Ce - M\zeta] = -\omega^2 \rho_f \boldsymbol{u} + \omega^2 \frac{\rho_f}{\beta} \left(\alpha_\infty + \frac{\eta \beta F_i}{\rho_f k_0 \omega} \right) \boldsymbol{w} + \frac{\eta F_r}{k_0} i\omega \boldsymbol{w}$$

and thus the dynamic permeability and tortuosity are given by

$$k(\omega) = \frac{k_0}{F_r}, \alpha(\omega) = \alpha_\infty + \frac{\eta \beta F_i}{\rho_f k_0 \omega}. \tag{34}$$

Since F_i is asymptotically proportional to $\sqrt{\omega}$, the second term in the formula for $\alpha(\omega)$ goes to zero. Likewise $F_r(0) = 1$ This justifies the identification of α_∞ and k_0 with the Biot-Stoll tortuosity parameter α and permeability parameter k in (31). Figure 12 shows $k(\omega)$ and $\alpha(\omega)$ for the sand of SAX99.

2.5.2 The viscosity correction factor for distributed pore sizes

Yamamoto and Turgut [45] assume that the pore sizes are distributed according to a density function $e(r)$ with
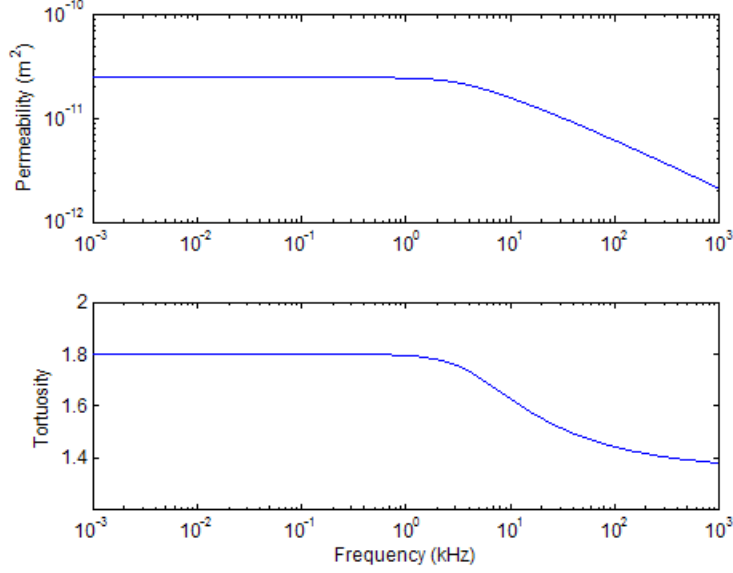
$$\int_0^\infty e(r) dr = 1.$$

Figure 12: Dynamic permeability and poresize given by formulae (34) for the parameters of Table 1, Column 4.

In their scheme permeability is related to the pore size distribution by

$$k_c = \frac{\beta}{8} \int_0^\infty r^2 e(r) dr, \, k_f = \frac{\beta}{3} \int_0^\infty r^2 e(r) dr \qquad (35)$$

for cylindrical and flat pores respectively. Note that this yields the formulas (20) and (22) for the case of a single pore size $e(r) = \delta(r - a)$.

For cylindrical pore ducts the force on the walls per unit volume is (see (16),(24),(26))

$$\int_0^\infty \frac{2\tau(r, \omega)}{r} e(r) dr = \int_0^\infty \frac{2}{r} \frac{\eta \chi(\omega) X}{i\omega} T\left(\chi(\omega)r\right) e(r) dr,$$

while the average velocity from (25) is

$$\int_0^\infty \langle V \rangle (r, \omega) e(r) dr = \int_0^\infty \frac{X}{i\omega} \left(1 + \frac{2i}{r\chi(\omega)} T(\chi(\omega)r)\right) e(r) dr.$$

Using (16) this gives

$$d = \frac{2\eta\chi(\omega) \int_0^\infty \frac{1}{r} T\left(\chi(\omega)r\right) e(r) dr}{\beta \int_0^\infty \left(1 + \frac{2i}{r\chi(\omega)} T(\chi(\omega)r)\right) e(r) dr}. \qquad (36)$$

21

Observe that for the case of Poiseuille flow we have from (21),(19) and (35)

$$d = \frac{\int_0^\infty \frac{2\tau(r,\omega)}{r} e(r)dr}{\beta \int_0^\infty \langle V \rangle (r,\omega) e(r)dr} = \frac{8\eta \int_0^\infty e(r)dr}{\beta \int_0^\infty r^2 e(r)dr} = \frac{\eta}{k_c}$$

and thus the expression for d has the expected limit as $\omega \to 0$.

Yamamoto and Turgut suggest a ϕ-normal distribution for pore size

$$f(\phi) = \frac{1}{\sigma_\phi \sqrt{2\pi}} \exp\left(-\frac{(\phi - \mu_\phi)^2}{2\sigma_\phi^2}\right), -\infty < \phi < \infty. \tag{37}$$

Phi units are defined by $\phi = -\log_2 r$ where r is measured in millimeters. In this case (36) becomes

$$d = \frac{2\eta \chi(\omega) \int_{-\infty}^\infty \frac{1}{r(\phi)} T\left(\chi(\omega) r\left(\phi\right)\right) f\left(\phi\right) d\phi}{\beta \int_{-\infty}^\infty \left(1 + \frac{2i}{r(\phi)\chi(\omega)} T(\chi(\omega) r\left(\phi\right))\right) f\left(\phi\right) d\phi}.$$

For $\overline{d} = d_r - id_i$ this gives the equations

$$\alpha(\omega) = \alpha_\infty + \frac{d_i \beta}{\omega \rho_f}, k(\omega) = \frac{\eta}{d_r} \tag{38}$$

for the dynamic tortuosity and permeability.

For the ϕ-normal distribution (37) the integral in (35) can be computed exactly, giving the permeability

$$k = \frac{\beta}{n_p} 2^{-2\mu_\phi} \exp(2(\sigma_\phi \ln 2)^2) 10^{-6} \, \text{m}^2$$

where $n_p = 3$ or 8 for the case of flat or cylindrical pores respectively. Thus for given k and σ_ϕ

$$\mu_\phi = -\frac{1}{2\ln 2} \ln\left(\frac{10^6 k n_p}{\beta} \exp(-2(\sigma_\phi \ln 2)^2)\right). \tag{39}$$

Since the pore size parameter is no longer used, there is not an increase in the number of parameters from the basic Biot-Stoll model, as long as one accepts the formulas (35). However values for the parameters μ_ϕ and σ_ϕ are not readily available. Yamamoto and Turgut [45] cite only one instance of direct measurement of pore size distribution, "Eagle River sand", for which $\mu_\phi \approx 5.75, \sigma_\phi \approx 1.5$ phi units.

Figure 13 shows how varying the standard deviation σ_ϕ of the pore size distribution affects the dynamic permeability and tortuosity computed from (38) (cf. Figure 12). The other parameters used were the those of Table 1, Column 4. For a fixed value of permeability increasing σ_ϕ decreases dynamic permeability and increases dynamic tortuosity with the changes being most pronounced at high frequencies for permeability and low frequencies for tortuosity. Figure 14 shows that the effect of increasing σ_ϕ on compressional wave speed and attenuation is to make the sediment behave more like a viscoelastic solid, that is, it is less dispersive with respect to wave speed and closer to log-linear with resect to attenuation.
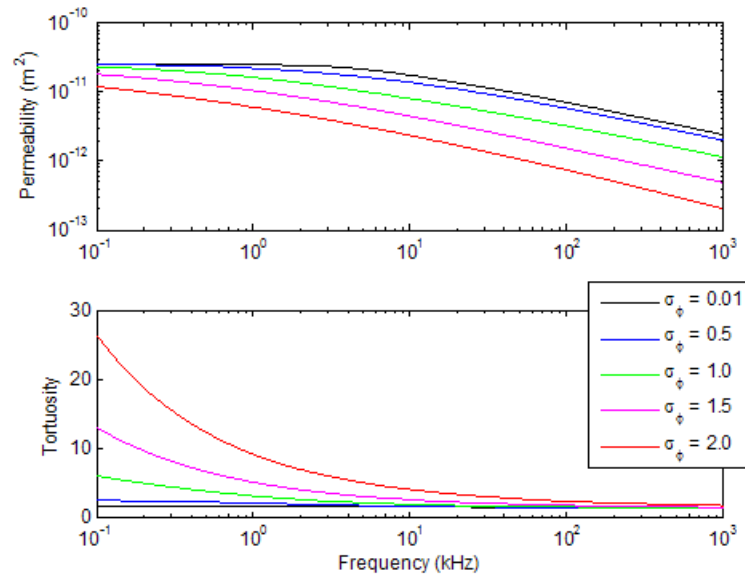
22

Figure 13: Effect on dynamic permeability and tortuosity of distributed pore sizes. The permeability was held constant, and the mean pore size was computed from (39).
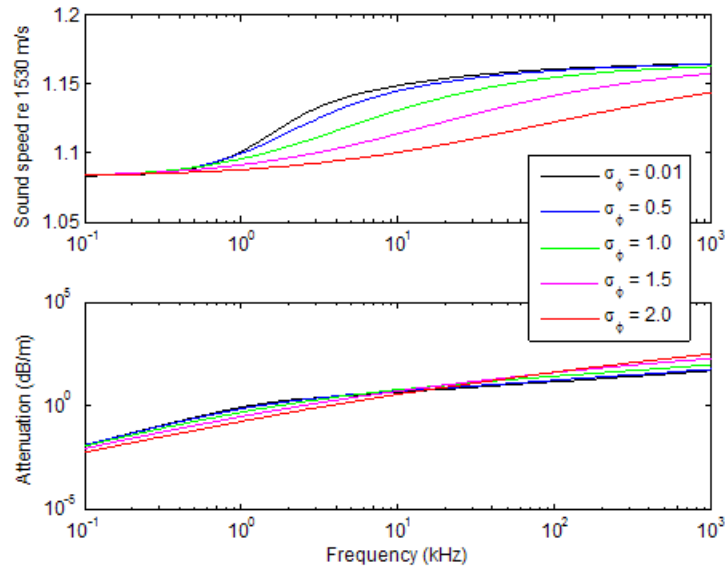
Figure 14: Effect on compressional wave speed and and attenuation of distributed pore sizes. The permeability was held constant, and the mean pore size was computed from (39).

2.5.3 Incorporation of "squirt flow"

Biot's modelling of viscoelastic forces at the granular level is discussed above in Section 2.4. Recently Chotiros and Isakson [17] have proposed frequency dependent forms for the moduli K_b^* and μ^* based on similar considerations. They take the region between two sand grains to consist of an area of solid contact and a gap into and out of which fluid can flow when the frame is subjected to expansion and compression (Figure 15). Following Dvorkin and Nur [18], they term this "squirt flow".The solid contact is modelled as a spring of modulus K_c and the effect of the flow in the gap, which will depend on the compressibility of the fluid and the resistance to radial expansion normal to the direction of the force is treated as a serial spring-dashpot (Maxwell) element with modulus K_y and damping constant η_y. The two mechanisms are assumed to act in parallel resulting in what is referred to in viscoelastic theory as the standard linear element (Figure 16(c)). Under a shearing force the absence of fluid loading for shear causes the viscoelastic element to simplify to a Kelvin-Voigt element with modulus G_c and damping constant η_s (Figure 16(d)). The effective moduli for the two types of elements undergoing time-harmonic oscillations $e^{-i\omega t}$ are (cf. Gittus [19], for instance)

$$K_b^* = K_c + \frac{K_y}{1 + i(\omega_k/\omega)} \tag{40}$$

$$\mu^* = G_c \left(1 - i\frac{\omega}{\omega_\mu} \right)$$

$$\omega_k = \frac{K_y}{\eta_y}, \omega_\mu = \frac{G_c}{\eta_s}.$$

As indicated in (40), Chotiros and Isakson identify these effective moduli with the Biot-Stoll parameters K_b^* and μ^*. Their argument for this is that the compressibility of the frame minerals is much less than that of the fluid and thus storage and loss mechanisms modelled by the two viscoelastic elements will predominate. They term the resulting modified Biot model the "Biot model with grain contact squirt flow and shear drag" (BICSQS).

The zero-frequency values K_c and G_c of the two moduli are assumed to be related by an equation of elasticity[4]

$$K_c = \frac{2}{3} G_c \frac{1 + \nu}{1 - 2\nu}$$

where ν is the Poisson ratio and thus the four independent Biot-Stoll parameters $\text{Re}\, K_b^*, \text{Im}\, K_b^*, \text{Re}\, \mu^*, \text{Im}\, \mu^*$ are replaced by the five parameters G_c, K_y, ν and the two relaxation frequencies

$$f_k = \frac{\omega_k}{2\pi}, f_\mu = \frac{\omega_\mu}{2\pi}.$$

---

[4]The of use such elastic relations has been challenged by Chotiros [15] on the grounds that an unconsolidated sediment is not a Hookean elastic solid, as is assumed in the Biot model. In this instance the parameter K_c turns out to have too little effect on the model's predictions to test the validity of this criticism, however.
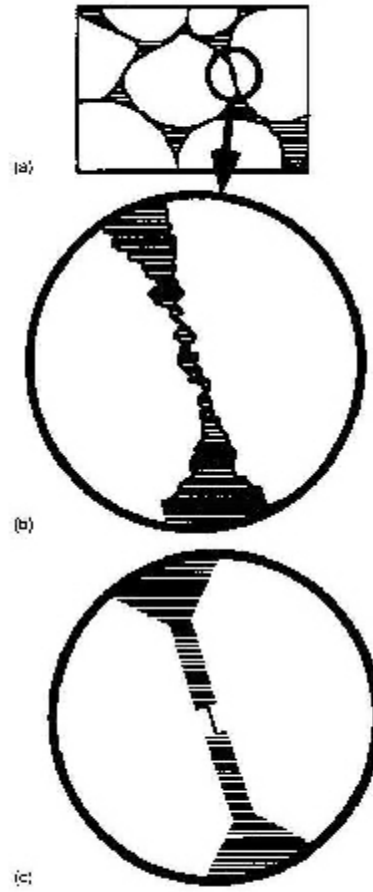
FIG. 3. Idealization of the grain-grain contact
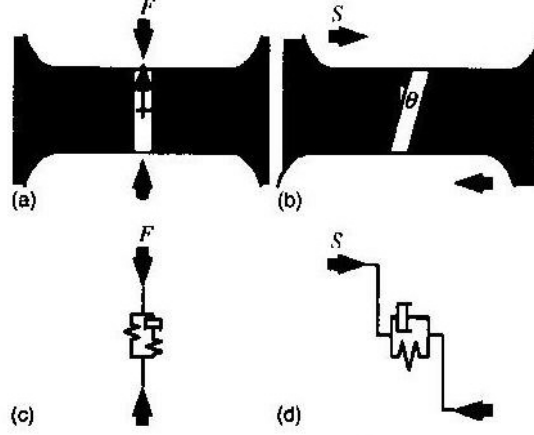
Figure 15: From [17].

26

FIG. 4. Grain contact models of (a) compression, (b) shear, and their equivalents (c) and (d).

Figure 16: From [17].

Comparing Chotiros and Isakson's equation $(40)_1$ with Biot's equation (28), we see that they are mathematically identical upon setting the compressibility κ_0 and the higher mode moduli $a_n, n > 1$ to zero and making the identifications $\kappa_1 = K_c^{-1}, a_1 = K_y, r_1 = \omega_k$. Thus while Biot does not state explicitly what the compressibilities κ_0 and κ_1 mean physically, if we assume that κ_0 represents the compressibility of the sand grains and κ_1 represents the compressibility of the solid contact region and assume as Chotiros and Isakson do that $\kappa_1 \gg \kappa_0$ then the two models are both physically and mathematically similar. Biot's model does not specifically mention resistance to radial flow as a damping mechanism, however. Likewise Chotiros and Isakson's equation for the shear modulus $(40)_2$ is Biot's equation (29) with $\mu_0 = G_c, s \approx 1, a = \mu_0 \omega_\mu^{-s}$, though the assumed physical mechanisms are different.

Because the speed of shear waves is controlled almost exclusively by the real part of μ^* and the parameters affecting the density of the seabed, the modulus G_c can be computed from a measured value of the shear wave speed, however there is no obvious way of determining the remaining parameters other than using them to fit observed data such as that displayed in Figures 1 and 2. Figures 17 and 18 indicate the influence of the four parameters K_y, ν, f_k and f_μ on compressional wave speed and attenuation in the case of the SAX99 sand (Table 1, Column 4) when they are varied about $K_y = 1$ GPa, $\nu = 0.15, f_k = 10$ kHz and $f_\mu = 50$ kHz. Poisson ratios in the range $[0.05, 0.25]$ have little effect on either speed or attenuation in the frequency range 100 Hz to 1 MHz. None of the four parameters have much effect below 1 kHz. The shear relaxation frequency
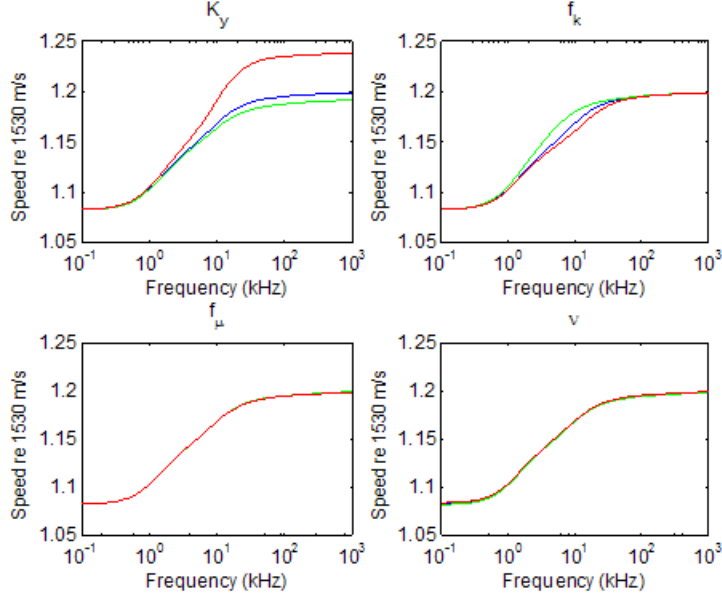
27

Figure 17: The effect on compressional wave speed of varying four parameters in the BICSQS model: $K_y = 1 \pm 0.2$ GPa, $f_k = 10 \pm 5$ kHz, $f_\mu = 50 \pm 25$ kHz, $\nu = 0.15 \pm 0.1$. Green, blue and red curves correspond to the lower, middle and upper values respectively.

f_μ is influential only on attenuation in the upper range of frequencies. The bulk modulus K_y and the bulk relaxation frequency influence wave speed in the middle to high range of frequencies and attenuation in the middle range.

As discussed above, Biot proposed models of viscoelastic loss that are, at least mathematically, generalizations of the BICSQS model. Figures 19 and 20 indicate the influence of the other parameters and of air bubble resonance. It was assumed in (28) that

$$\kappa_0 + \kappa_1 = \left(\frac{2}{3} G_c \frac{1 + \nu}{1 - 2v} \right)^{-1}.$$

Increasing the compressibility κ_0 lowered the compressional wave speed in the high frequency range and thus countered the effect of $\kappa_1 = K_y^{-1}$. Likewise lowering s in equation (29) counteracted the effect on attenuation of increasing f_μ, however it also caused wave speed to rise slightly at high frequencies. Thus if one is seeking to change the predictions of the Biot model in order to produce better agreement with data, the approximations $\kappa_0 \approx 0, s \approx 1$ which lead to the BICSQS model seem reasonable. The second and third modes in (28) cause wave speed to rise slightly at higher frequencies. In computing the modes it was assumed that in equation (28) $a_n = a_1/(2n - 1)$ and $k_n = (2n - 1)^2 k_1$ with
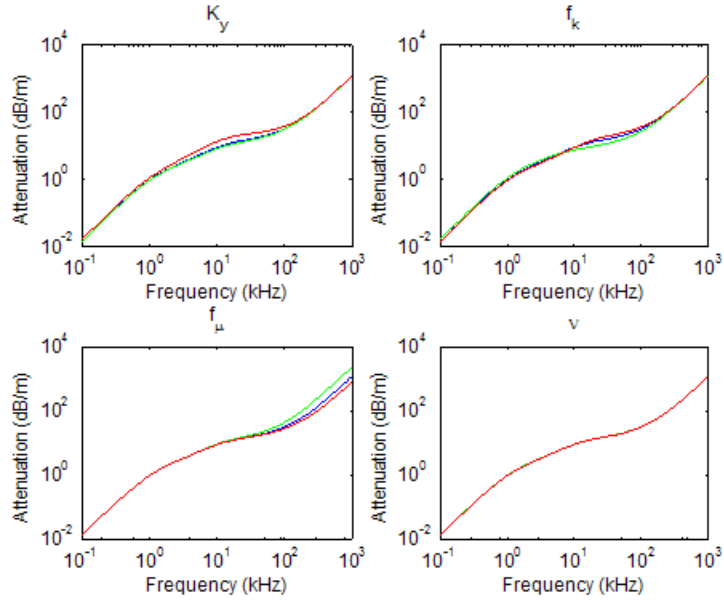
28

Figure 18: The effect on compressional wave attenuation of varying four parameters in the BICSQS model: $K_y = 1 \pm 0.2$ GPa, $f_k = 10 \pm 5$ kHz, $f_\mu = 50 \pm 25$ kHz, $\nu = 0.15 \pm 0.1$. Green, blue and red curves correspond to the lower, middle and upper values respectively.
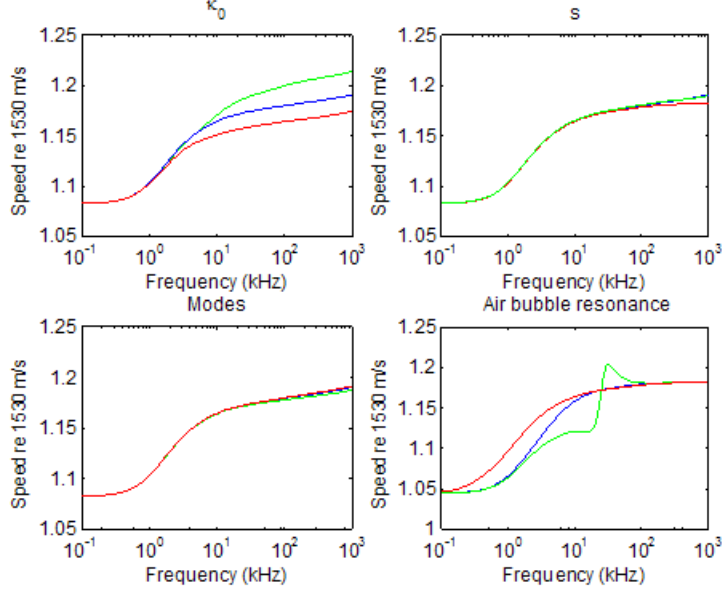
Figure 19: Effect upon compressional wave speed assuming the more general equations (28), (29) and (30) given by Biot in [8]. It is assumed that $K_y = 10^9, f_k = 10\,\text{kHz}, f_\mu = 50\,\text{kHz}$. In the upper left panel $s = 0.75$ and green, blue and red are $\kappa_0 = 10^{-9\pm1}$ in ascending order. In the upper right panel $\kappa_0 = 10^{-9}$ and $s = 0.75 \pm 0.25$ with the same color ordering. In the lower right panel $\kappa_0 = 10^{-9}, s = 0.75$ and green, blue and red correspond to using 1,2 and 3 modes in equation (28) respectively. In the lower right panel $\kappa_0 = 10^{-9}, s = 1.0$ and $b_a = 10^5, 10^6, 10^7$ for green, blue and red respectively.

$a_1 = \omega_k, k_1 = K_y$. For the air bubble resonance it was assumed $c_0 = (1-\phi)K_f^{-1}$ and $k_a^{-1} = \phi K_a^{-1}$ so that at angular frequency $\omega = 0$ equation (30) gives the Reuss model composite compressibility

$$c = (1 - \phi)K_f^{-1} + \phi K_a^{-1}. \qquad (41)$$

The gas volume fraction was taken to be $\phi = 5 \times 10^{-6}$. This sufficed to give agreement with the measured low frequency wave speeds shown in Figure 1. The bulk modulus of air was taken to be $K_a = 0.142$ MPa, based on a sound speed of 343 m/s and a density of 1.21 kg/m^3. The approximate resonant frequency was taken to be $f_a = 25\,\text{kHz}$ and the mass m_a in (30) was computed from $m_a = k_a/(2\pi f_a)^2$. The damping parameter b_a controls how rapidly the wave speed changes with respect to frequency.
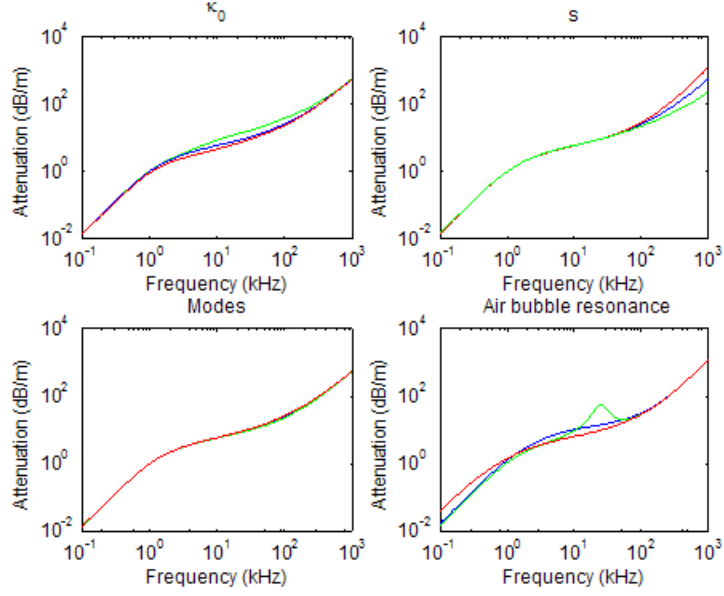
Figure 20: Effect upon compressional wave attenuation assuming the more general equations (28), (29) and (30) given by Biot in [8]. It is assumed that $K_y = 10^9, f_k = 10\,\text{kHz}, f_\mu = 50\,\text{kHz}$. In the upper left panel $s = 0.75$ and green, blue and red are $\kappa_0 = 10^{-9\pm1}$ in ascending order. In the upper right panel $\kappa_0 = 10^{-9}$ and $s = 0.75 \pm 0.25$ with the same color ordering. In the lower right panel $\kappa_0 = 10^{-9}, s = 0.75$ and green, blue and red correspond to using 1,2 and 3 modes in equation (28) respectively. In the lower right panel $\kappa_0 = 10^{-9}, s = 1.0$ and $b_a = 10^5, 10^6, 10^7$ for green, blue and red respectively.

Sediment	ρ_r	K_r	β	k	α	a
Fine Sand	2670	4.0×10^{10}	0.43	3.12×10^{-14}	1.25	1.20×10^{-6}
Medium Sand	2690	3.2×10^{10}	0.385	2.5×10^{-11}	1.35	6.28×10^{-5}
Gravel	2680	4.0×10^{10}	0.30	2.58×10^{-10}	1.25	1.31×10^{-4}
Silty Sand	2670	3.8×10^{10}	0.65	6.33×10^{-15}	3.0	4.25×10^{-7}
Silty Clay	2680	3.5×10^{10}	0.68	5.2×10^{-14}	3.0	1.24×10^{-6}

Table 2: Biot-Stoll parameters for five different sediment types.

Symbol	Estimate
ρ_f	1000
K_f	2.4×10^9
η	1.01×10^{-3}

Table 3: Typical fluid parameters for the Biot-Stoll model.

2.6   Confirmation of Biot's equations

The Biot model is often described as phenomenological: it does not delve into underlying causes. It is worth noting however that Burridge and Keller [14] did succeed in deriving Biot's macroscopic equations from the microstructure, that is, using the linearized equations of elasticity and fluid motion by means of the mathematical technique of two-scale homogenization under the assumptions that the medium was macroscopically homogeneous and that microstructure scale was much smaller than the macroscopic scale. They also demonstrated the existence of a strain energy function, as postulated by Biot.

3   Determination of the Biot-Stoll parameters

To make predictions using the Biot-Stoll model the thirteen parameters in Table 1 must be determined. Historically this has been done eclectically by a combination of handbook values, empirical formulas, *in situ* measurements and reference to the literature. The exception to this is SAX99 in which attempts were made to measure most of the Biot-Stoll parameters at a site near Fort Walton Beach Florida (Table 1). In order to examine the predictions of the Biot model it is useful to have parameters for a variety of seabeds. Values for six Biot-Stoll parameters for five different sediments are given in Table 2. The medium sand parameters are those of Table 1 for the sand examined in SAX99. The fine sand, silty clay and gravel parameters are from Holland and Brunson [23]. The parameters for silty sand are from Beebe, McDaniels and Rubano [2]. For the parameters other than medium sand we will use the fluid parameters in Table 3.

As can be seen in Table 1 some of the Biot-Stoll parameters can be determined quite accurately and vary little in the context of water-saturated seabeds. Let us examine some of the parameters which are more difficult to determine.

3.1 Porosity

In SAX99 porosity was estimated using several different techniques: gravimetric determination produced a 95% confidence interval [0.359,0.387]. Image analysis produced a range of estimates from 0.34 to 0.48. Gravimetric analysis of resin impregnated cores resulted in estimates ranging from 0.41 to 0.52. Two separate conductivity probes *in situ* yielded 95% confidence intervals of [0.364,0.383] and [0.363,0.394]. These and all subsequent values for SAX99 are from Williams *et al.* [44]. Historically porosity has been measured from core and grab samples. The wide range of values generated by the different techniques used in SAX99 is a surprise since porosity has usually not been regarded as being subject to great uncertainty.

3.2 Tortuosity

For SAX99 the following definition of tortuosity was used: the square of the ratio of the minimum length of a contiguous path through the pore space between two points to the linear distance between the points. Tortuosity was estimated by image analysis of resin-impregnated divers cores.

Traditionally experimenters have simply followed the suggestion of Stoll [37] and used $\alpha = 1.25$ for highly permeable sediments and $\alpha = 3.0$ for silty, less permeable, sediments (see Table 2).

3.3 Fluid bulk modulus

The bulk modulus of the seawater was calculated from

$$K_f = \rho_f c_o^2$$

where c_o is the sound speed of water in the ocean. The density ρ_f was calculated based on the temperature and salinity of the water. It was felt that assuming the properties of the pore water were the same as that of the ocean water above introduced little error ([44]). The result was the rather narrow range of values shown in Table 1.

Chotiros and Isakson [17] have recently challenged this range, arguing that the effective bulk modulus may have been significantly lower, 2.15 GPa versus 2.4 GPa, due to the presence of air bubbles in the pore space. As evidence for this they cite the attempts to measure gas content of sediment cores described in Richardson *et al.* [33] which resulted in measurements ranging from 20 to 150 ppm. The authors of [33] state however that "All of these values indicate smaller volumes of gas than the system was designed to resolve. We cannot on the basis of these data reject the hypothesis that the gas content is zero." As indicated in Figure 19 a very small gas fraction, around 5 ppm, would suffice to lower the low frequency wave speed the measured values shown in Figure 1 if the Reuss model (41) is assumed for the effective fluid modulus[5].

---

[5]Chotiros and Isakson state that a value of 35.4 ppm would give their chosen value of

3.4 Permeability and the pore size parameter

For SAX99 a constant head technique on divers cores produced a 95% confidence interval of $[2.1, 4.5] \times 10^{-11} \, \mathrm{m}^2$ for permeability. Image analysis of resin impregnated cores produced a confidence interval of $[0.75, 4.8] \times 10^{-11} \, \mathrm{m}^2$. An *in situ* constant head technique produced a confidence interval of $[0.3, 6.1] \times 10^{-11} \, \mathrm{m}^2$. Thus the estimates spanned more than a decade. As mentioned above Williams *et al.* [44] used equation (33) to determine the pore size parameter from the permeability and tortuosity.

Traditionally experimenters have calculated permeability from statistics on grain size distribution via a variety of empirical formulae. For instance Holland and Brunson [23] used the Kozeny-Carmen equation

$$k = \frac{\beta^3}{KS_0^2(1-\beta)^2} \tag{42}$$

where K is an empirical constant which is approximately 5 for spherical grains and S_0 is the surface area per unit volume of the particles. The latter parameter was calculated as

$$S_0 = \sum_n \frac{6}{d_n} w_n$$

from a discrete set (d_n, w_n) of grain sizes d_n and proportions w_n of total volume obtained by sorting the sample. Beebe *et al.* [2] used a different empirical relation due to Krumbien and Monk [27] which depends upon the mean M_ϕ and standard deviation σ_ϕ of grain sizes in ϕ units

$$k = 7.6d^2 e^{-1.31\sigma_\phi} \times 10^{-10} \, \mathrm{m}^2 \tag{43}$$

where $d = 2^{-M_\phi}$ mm is the mean grain diameter. Hovem and Ingram [24] identified the pore size parameter with twice the hydraulic radius to arrive at

$$a = \frac{d\beta}{3(1-\beta)} \times 10^{-3} \, \mathrm{m} \,. \tag{44}$$

Permeability is then calculated from the Kozeny-Carmen formula written as

$$k = \frac{\beta a^2}{4K} \,. \tag{45}$$

Assuming that grain sizes have a ϕ-normal distribution (37) Chotiros [15] arrives at the formula

$$a = \frac{\beta}{3(1-\beta)} \exp(y_0 + \sigma_y^2) \times 10^{-3} \, \mathrm{m} \tag{46}$$

$K_f = 2.15$ GPa, but do not state what model this is based upon. This may be a misstatement since the rest of their gas fraction values are roughly consistent with the Reuss-Voigt-Hill model which averages the Ruess model value $K_f^{-1} = (1 - \phi)K_w^{-1} + \phi K_a^{-1}$ with the Voigt model value $K_f = (1 - \phi)K_w + \phi K_a$ where K_w and K_a are the bulk moduli of water and air respectively.

β	M_ϕ	σ_ϕ	k_{KM}	k_{HI}	k_ϕ	k_C
0.65	6.37	2.19	6.3×10^{-15}	1.8×10^{-12}	1.8×10^{-10}	1.8×10^{-14}
0.47	3.0	1.7	1.2×10^{-12}	3.2×10^{-11}	5.2×10^{-10}	2.0×10^{-12}
0.38	0.85	0.83	7.9×10^{-11}	2.4×10^{-10}	4.7×10^{-10}	1.3×10^{-10}
0.38	0.5	1.0	1.0×10^{-10}	4.0×10^{-10}	1.0×10^{-9}	1.5×10^{-10}
0.38	1.2	0.6	6.6×10^{-11}	1.5×10^{-10}	2.1×10^{-10}	1.1×10^{-10}

Table 4: Permeabilities calculated from the same grain size statistics using four different formulas.

where $y_0 = -M_\phi \ln 2, \sigma_y = -\sigma_\phi \ln 2$. Finally working from the hydraulic radius concept Chotiros [15] arrived at a formula for pore size which differs from (46) only by a minus sign

$$a = \frac{\beta}{3(1 - \beta)} \exp(y_0 - \sigma_y^2) \times 10^{-3} \, \mathrm{m} \,. \tag{47}$$

Table 4 shows the result of calculating permeability using formulas (43), (44), (46), and (47) (under the headings $k_{KM}, k_{HI}, k_\phi, k_C$ respectively). All of the grain size statistics and porosities were taken from [2], Table 2. As can be seen the four formulas lead to widely differing values for permeability, especially as the grain size gets smaller and the dispersion larger. Thus unfortunately the value of this very important parameter is elusive.

3.5 Frame response parameters

The frame response parameters are the shear modulus μ^* and the frame bulk modulus K_b^*. They are usually taken to be complex valued in order to account for losses due to intergranular friction. There are various empirical formulas for calculating them. Bryan and Stoll [10] assume a functional form for the shear modulus

$$\mu_1 = p_a a \exp(-b\varepsilon)(\sigma_0/p_a)^n \tag{48}$$

where p_a is the atmospheric pressure,

$$\varepsilon = \frac{\beta}{1 - \beta}$$

is the voids ratio, and the mean effective stress due to over-burden pressure is

$$\sigma_0 = \frac{1 + 2K_0}{3} \int_0^z g(1 - \beta(z))(\rho_r - \rho_f)dz \tag{49}$$

where z is the depth into the sediment, K_0 is the coefficient of earth pressure at rest, which is typically taken to be 0.5, and g is the acceleration due to gravity. Based on statistical regressions on laboratory results Stoll arrived at the values $a = 2526, b = 1.504$ and $n = 0.448$. As field tests tended to lead to somewhat higher values for the shear modulus than laboratory results, Stoll [38] suggested

35

an empirical modification $\mu = FF \cdot \mu_1$ where $FF = 2$. Badiey, Cheng and Mu [1] have a similar formulation

$$\mu = a \times 10^5 \varepsilon^{-b} \sqrt{\sigma_0} \tag{50}$$

with $a = 6.56, b = 1.10$ for sand dominant sediments, $a = 2.05, b = 1.29$ for clay dominant sediments and $a = 2.44, b = -1.628$ for general (indeterminate) sediments. The complex moduli are then calculated from

$$\mu^* = (1 + i\Delta_\mu/\pi)\, \mu \tag{51}$$
$$K_b^* = \frac{2\,(1+\nu)}{3\,(1-2\nu)} \mu \left(1 + i\Delta_{K_b}/\pi\right)$$

where Δ_{K_b} and Δ_μ are the log decrements for compressional and shear vibrations and ν is the Poisson ratio.

Figures 21-23 compare the predictions for the variation of shear wave speed with respect to depth into the sediment given by the Bryan-Stoll and Badiey-Cheng-Mu empirical formulas for three of the sediments in Table 2 for which there is experimental data. The data points for Figure 21 are from [33] and those for Figures 22 and 23 from [34]. How the shear wave speeds are calculated will be discussed in Section 4.1. It should be noted that the equations of motion were derived under the assumption that the model parameters were constant and thus use the equations with depth-varying moduli constitutes an approximation of uncertain accuracy. Be that as it may, Figures 21-23 indicate that the Bryan-Stoll formulation with either $FF = 1$ (silty clay and fine sand) or $FF = 2$ (medium sand) best fits the data. Possibly the field factor is needed only for highly permeable sediments.

The shear wave speed is significantly affected by only three Biot-Stoll parameters: the shear modulus $\mu = \mathrm{Re}\,\mu^*$; the porosity β; and the grain density ρ_r [16]. In SAX99 the shear wave speed was measured in the range 97 to 147 m / s and the average value $c_s = 120$ was used in the formula $\mu = \rho c_s^2$.

4 Predictions of the Biot-Stoll model

In the examples of the predictions of the Biot-Stoll model in this section the frame response moduli were computed from (51) at a depth of $z = 0.2\,\mathrm{m}$ using the empirical formula of Bryan and Stoll given above. The required Poisson ratios and log decrements, and field factors are given in Table 5.

4.1 Wave speed and attenuation

Upon taking the divergence of both equations in (14) and assuming time harmonic vibrations $e(x, y, z, t) = e(x, y, z)e^{-i\omega t}, \ldots$ we obtain

$$H\nabla^2 e - C\nabla^2 \zeta = -\omega^2 \rho e + \omega^2 \rho_f \zeta \tag{52}$$
$$C\nabla^2 e - M\nabla^2 \zeta = -\omega^2 \rho_f e + \left(\omega^2 m + i\omega d\right) \zeta.$$
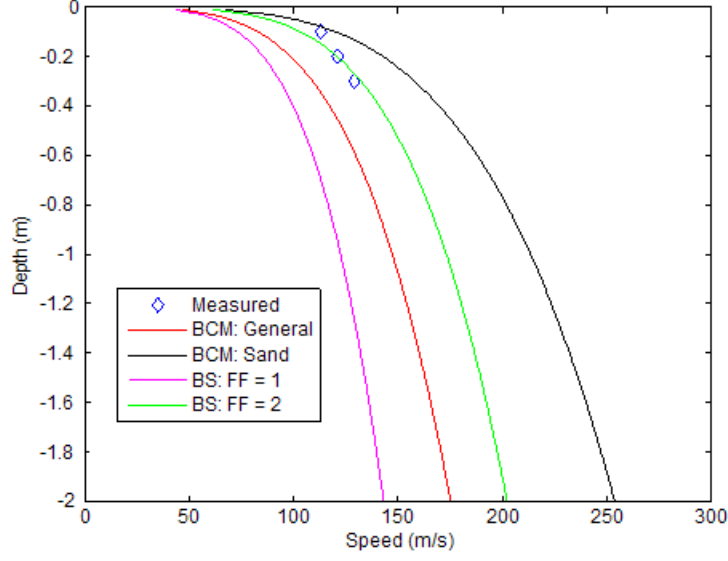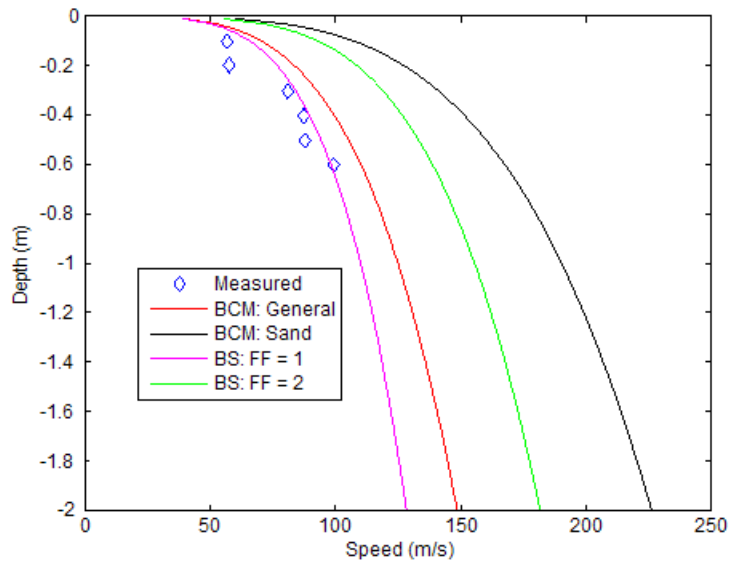
Figure 21: Predictions for the variation of shear wave speed with respect to depth for medium sand by four different empirical formulas for the shear wave modulus. The measured values are from [33]. The curves labeled "BCM: General" and "BCM: Sand" were calculated from (50) using the parameters given in the text. The curves labeled "BS: FF = 1" and "BS: FF = 2" were calculated from (48) with the indicated field factor.
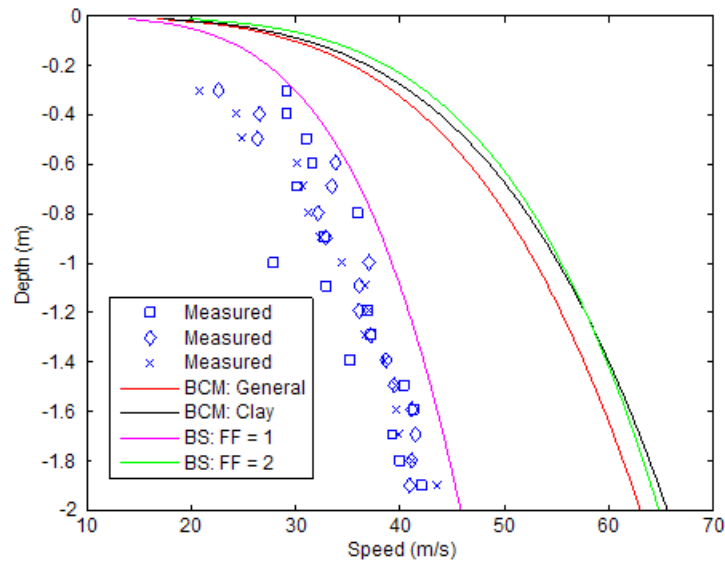
Sediment	ν	Δ_{K_b}	Δ_μ	FF
Fine sand	0.25	0.15	0.15	1
Medium sand	0.15	0.15	0.3	2
Gravel	0.25	0.15	0.15	2
Silty sand	0.25	0.1	0.1	1
Silty clay	0.25	0.5	0.5	1

Table 5: Poisson ratios and log decrements for five sediments.

Figure 22: Predictions for the variation of shear wave speed with respect to depth for fine sand by four different empirical formulas for the shear wave modulus. The measured values are from [34]. The curves labeled "BCM: General" and "BCM: Sand" were calculated from (50) using the parameters given in the text. The curves labeled "BS: FF = 1" and "BS: FF = 2" were calculated from (48) with the indicated field factor.

Figure 23: Predictions for the variation of shear wave speed with respect to depth for silty clay by four different empirical formulas for the shear wave modulus. The measured values are from [34]. The curves labeled "BCM: General" and "BCM: Clay" were calculated from (50) using the parameters given in the text. The curves labeled "BS: FF = 1" and "BS: FF = 2" were calculated from (48) with the indicated field factor.

Thus

$$\nabla^2 \begin{bmatrix} e \\ \zeta \end{bmatrix} + K \begin{bmatrix} e \\ \zeta \end{bmatrix} = \begin{bmatrix} 0 \\ 0 \end{bmatrix} \tag{53}$$

where

$$K = - \begin{bmatrix} H & -C \\ C & -M \end{bmatrix}^{-1} \begin{bmatrix} -\omega^2 \rho & \omega^2 \rho_f \\ -\omega^2 \rho_f & \omega^2 m + i\omega d \end{bmatrix}.$$

Upon taking the curl of both equations and assuming time-harmonic vibrations we obtain

$$\mu \nabla^2 \boldsymbol{\varphi} = -\omega^2 (\rho \boldsymbol{\varphi} - \rho_f \boldsymbol{\Phi}) \tag{54}$$
$$\mathbf{0} = -\omega^2 (\rho_f \boldsymbol{\varphi} - m \boldsymbol{\Phi}) + di\omega \boldsymbol{\Phi}$$

where $\boldsymbol{\varphi} = \boldsymbol{\nabla} \times \boldsymbol{u}$ and $\boldsymbol{\Phi} = \boldsymbol{\nabla} \times \boldsymbol{w}$. Solving the second equation for $\boldsymbol{\Phi}$ and substituting into the first equation gives

$$\nabla^2 \boldsymbol{\varphi} + k_s^2 \boldsymbol{\varphi} = \mathbf{0}$$

where

$$k_s = \sqrt{\frac{\omega^2 (\rho \omega m + i\rho d - \rho_f^2 \omega)}{(\omega m + id)\mu}}.$$

Finally solving the time-harmonic version of $(14)_2$ for $\boldsymbol{w}$ to obtain

$$\boldsymbol{w} = \frac{1}{\omega(\omega m + id)} \left[C\boldsymbol{\nabla} e - M\boldsymbol{\nabla}\zeta + \omega^2 \rho_f \boldsymbol{u} \right]$$

and substituting this result into $(14)_1$ leads to

$$\nabla^2 \boldsymbol{u} + A_1 \boldsymbol{\nabla} e + A_2 \boldsymbol{\nabla}\zeta + k_s^2 \boldsymbol{u} = \mathbf{0} \tag{55}$$

where

$$A_1 = \frac{(H - \mu)\omega m - C\omega\rho_f + (H - \mu)di}{(\omega m + id)\mu}$$
$$A_2 = \frac{M\rho_f \omega - Cm\omega - iCd}{(\omega m + id)\mu}.$$

There are three complex wave numbers k_1, k_2, k_s where k_1, k_2 are the square roots of the eigenvalues of K. Thus the Biot-Stoll model predicts two compressional waves as well as a shear wave. The two compressional waves are referred to as Type I and II or fast and slow waves. Figures 24 and 25 show the Biot-Stoll models predictions for Type I wave speed and attenuation for the five sediments of Table 2. Type I waves correspond to the compressional waves predicted by the Buckingham or elastic models, but for highly permeable sediments such as the gravel and SAX99 sediments, they are more dispersive with respect to frequency. The behavior of the attenuation with respect to frequency f for highly permeable sediments is roughly characterized as increasing like f^2
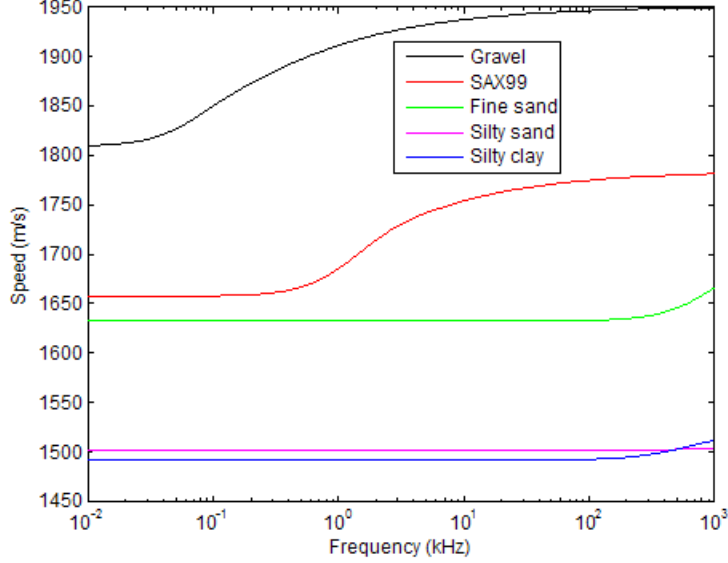
40

Figure 24: Biot model predictions for Type I compressional wave speeds for five sediments.

for low frequencies and $f^{1/2}$ for high frequencies, as opposed to f^1 in the Buckingham model. For less permeable sediments the predictions of the Biot model are similar to those of the elastic model. Figures 26-29 show the Biot model's predictions for Type II and shear wave speed and compressional attenuation for the five sediments of Table 2. Both waves have similar speeds. Type II waves for unconsolidated sediments are highly attenuated and have not been detected with certainty. See however Section 5.3.

4.2 Reflection and transmission at the ocean-sediment interface

4.2.1 The case of constant seabed parameters

The equations for reflection and transmission for the Biot model were originally worked out by Stoll and Kan [40]. Stern, Bedford and Milwater [36] have considered the case of depth-varying sediment properties. We will treat the case of constant properties, but in a way which can be extended in theory to the depth-varying case. Assuming an incident plane wave of amplitude one, pressure in the ocean has the form

$$P_o = e^{ik_x x} \left(e^{ik_z z} + R e^{-ik_z z} \right)$$

Figure 25: Biot model predictions for Type I compressional wave attenuation for five sediments.

where $k_x = (\omega/c_0)\cos\theta, k_z = (\omega/c_0)\sin\theta$, c_0 is the sound speed in water, the angle of incidence θ is measured from horizontal and the positive z-direction is into the sediment. The time-harmonic factor $e^{-i\omega t}$ has been discarded so that P_o will have the same form as the solutions to (53) and (55). Vertical displacement in the ocean is given by

$$U_{zo} = \frac{1}{\rho\omega^2}\frac{\partial P_o}{\partial z} = \frac{1}{\rho\omega^2}e^{ik_x x}\left(ik_z e^{ik_z z} - Rik_z e^{-ik_z z}\right).$$

For the ocean-sediment interface at $z = 0$, the following conditions are imposed:

$$U_{zo}(x,0) = \beta U_z(x,0) + (1-\beta)u_z(x,0) = u_z(x,0) - w_z(x,0) \qquad (56)$$
$$P_o(x,0) = \tau_{zz}(x,0)$$
$$P_o(x,0) = p_f(x,0)$$
$$\tau_{xz}(x,0) = 0.$$

These conditions represent continuity of displacement in the ocean with aggregate displacement in the sediment, continuity of normal pressure, continuity of fluid pressure, and vanishing of shear stress at the sediment surface.

Snell's law requires the solutions to (53) and (55) in the seabed have the form

$$\left[\begin{array}{c} e(x,z) \\ \zeta(x,z) \end{array}\right] = e^{ik_x x}\left[\begin{array}{c} e(z) \\ \zeta(z) \end{array}\right], \left[\begin{array}{c} u_x(x,z) \\ u_z(x,z) \end{array}\right] = e^{ik_x x}\left[\begin{array}{c} u_x(z) \\ u_z(z) \end{array}\right] \qquad (57)$$
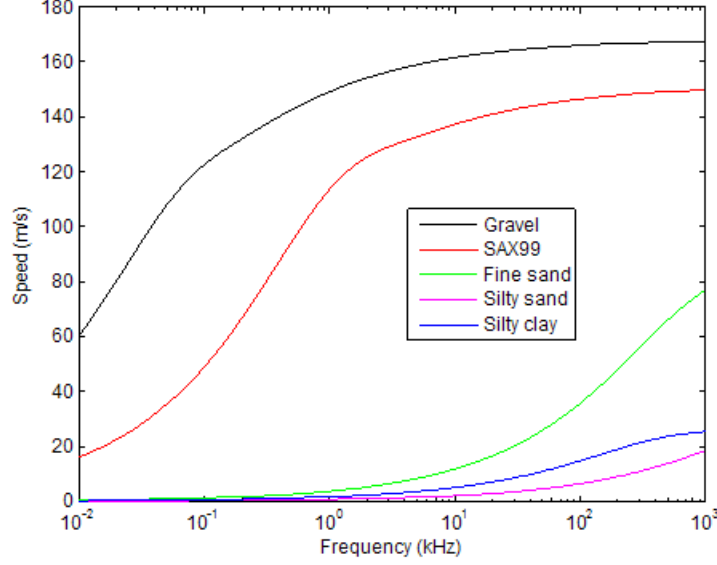
42

Figure 26: Biot model predictions for Type II compressional wave speeds for five sediments.

Substituting the first of these into (53) gives

$$\left[\begin{array}{c} e''(z) \\ \zeta''(z) \end{array} \right] + (K - k_x^2 I) \left[\begin{array}{c} e(z) \\ \zeta(z) \end{array} \right] = \left[\begin{array}{c} 0 \\ 0 \end{array} \right].$$

For a constant matrix K this system of differential equations has the solution

$$\left[\begin{array}{c} e \\ \zeta \end{array} \right] = C_1 E_1 e^{i\ell_1 z} + C_2 E_2 e^{i\ell_2 z} \tag{58}$$

where the wave numbers are given by

$$\ell_n = \sqrt{\lambda_n - k_x^2}, n = 1, 2$$

and λ_n, E_n are eigenvalues and eigenvectors of K. The branch cut for the square root is chosen so that $\text{Im}\, \ell_n > 0$. The exponentially growing components of the solution (58) involving $e^{-il_n z}$ have been discarded. Substituting the assumed form for $\boldsymbol{u}$ from (57) into (55) gives

$$\boldsymbol{u}'' + (k_s^2 - k_x^2)\boldsymbol{u} = -A_1 \boldsymbol{\nabla} e - A_2 \boldsymbol{\nabla} \zeta$$

where the right hand side is known by virtue of (58). This system has solutions of the form

$$u_x(z) = C_3 e^{i\ell_s z} + F_1 e^{i\ell_1 z} + F_2 e^{i\ell_2 z}, u_z(z) = C_4 e^{i\ell_s z} + +G_1 e^{i\ell_1 z} + G_2 e^{i\ell_2 z}$$

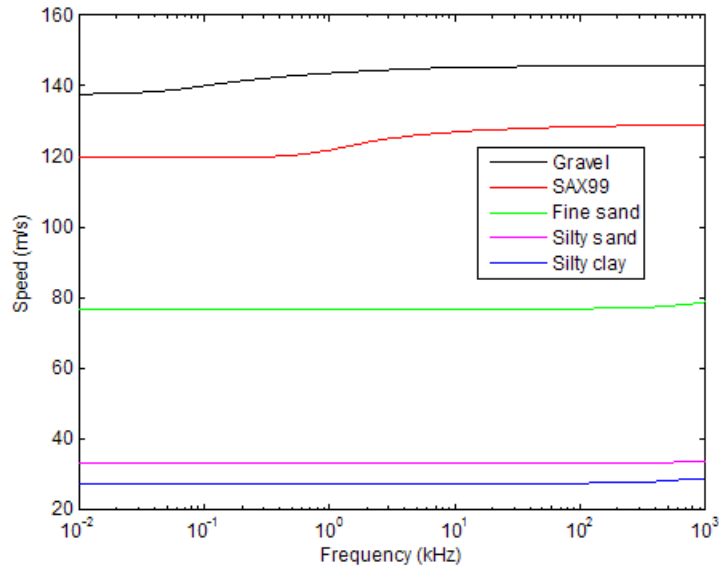Figure 27: Biot model predictions for Type II compressional wave attenuation for five sediments.

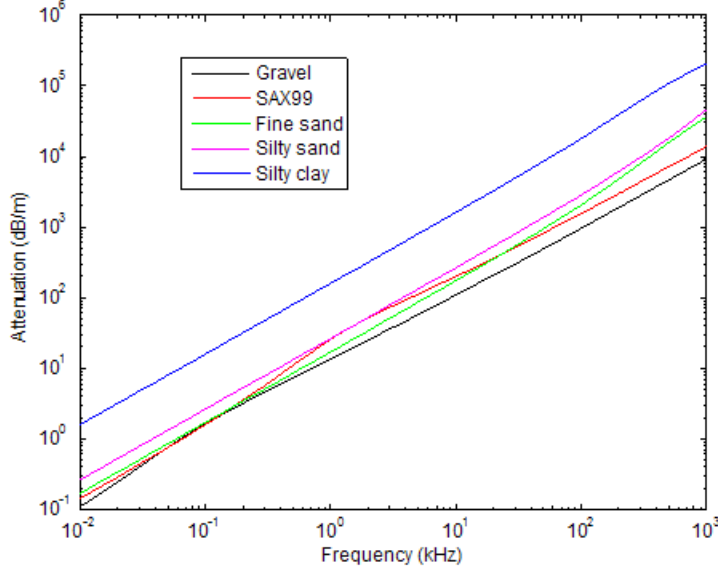Figure 28: Biot model predictions for shear wave speeds for five sediments.

44

Figure 29: Biot model predictions for shear wave attenuation for five sediments.

where F_1, F_2, G_1, G_2 are linear functions of C_1, C_2 and the components of the eigenvectors and the wave number is given by

$$\ell_s = \sqrt{k_s^2 - k_x^2}.$$

By equating the coefficients of $e^{i\ell_1 z}, e^{i\ell_2 z}, e^{i\ell_s z}$, the constants C_3 and C_4 can be related and the components of the eigenvectors determined. Thus the four sediments solutions $e, (z), \zeta(z), u_x(z), u_z(z)$ depend upon three arbitrary constants. The four interface conditions (56) now constitute a system of four linear equations which may be solved for C_1, C_2, C_3, R.

Figures 30 and 31 show that the Biot model does not predict a critical angle as does the fluid model, but it does predict a quasi-critical angle with a similar value. For instance the critical angle for the medium sand sediment of SAX99 was $30°$. Figures 32 and 33 show how the reflection coefficient varies with frequency at an incident angle of $5°$. Figure 34 shows how the reflection coefficient varies with frequency at different angles for the medium sand of Table 2.

Given that the Biot model predicts that transmission of energy into the seabed is possible at all angles, the question arises as to whether this might explain the instances of detection described in [41] during SAX99 of objects by waves incident at angles below the critical angle. Figure 31 indicates that at the incident angle of $5°$ and frequency $20\,\text{kHz}$ used in the experiment, the coefficient of reflection was about 0.95. Thus other explanations such as diffrac-
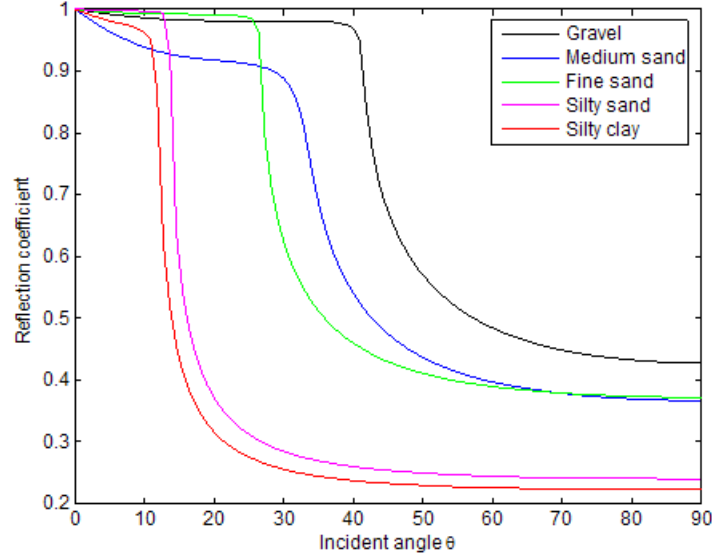
Figure 30: Biot model's prediction for the coefficient of reflection. The frequency is 20 kHz and the sound speed in water is 1460 m / s, which is below the compressional wave speeds of all of the sediments.

tion or refraction of energy into the sediment by surface roughness or scattering of evanescent waves by volume heterogeneity within the sediment seem more plausible [41], however see Section 5.3.

5 Difficulties with and controversies about the Biot-Stoll model

5.1 Can the parameters be determined accurately enough?

The Biot model predictions for the SAX99 data shown in Figures 1 and 2 are best fit predictions and thus only can be obtained *a posteriori*. It is worthwhile to inquire what is the range of possible predictions, given the parameter ranges in Table 1, Column 3. Of the Biot-Stoll parameters for which there is much uncertainty only four, porosity, permeability, grain bulk modulus, and tortuosity, have much influence on Type I compressional wave speeds and attenuation[6]. Figures 35 and 36 show the influence of each of these parameters separately on

---

[6] If one accepts the air bubble hypothesis of Chotiros and Isakson [17], then fluid bulk modulus should be added to this list. See Section 3.3 for a discussion of this hypothesis and Section 5.2.2 to see the effect of varying the fluid bulk modulus.
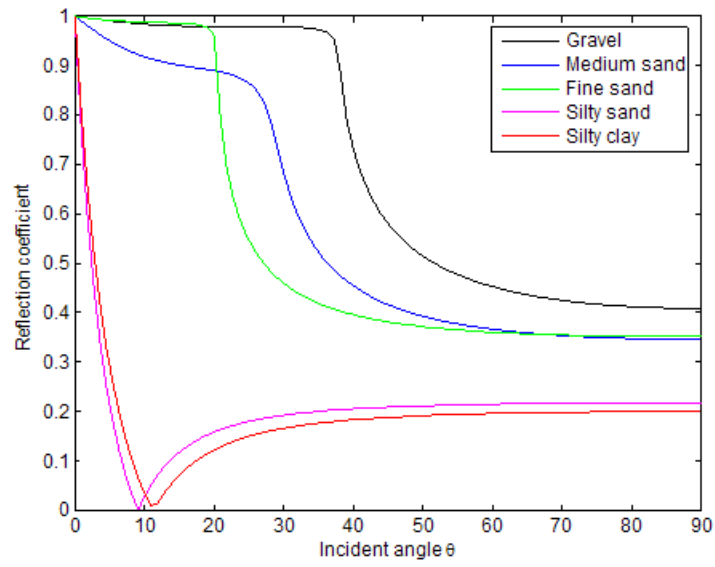
Figure 31: Biot model's prediction for the coefficient of reflection. The frequency is 20 kHz and the sound speed in water is 1530 m / s, which is above the compressional wave speeds of the two silty sediments.
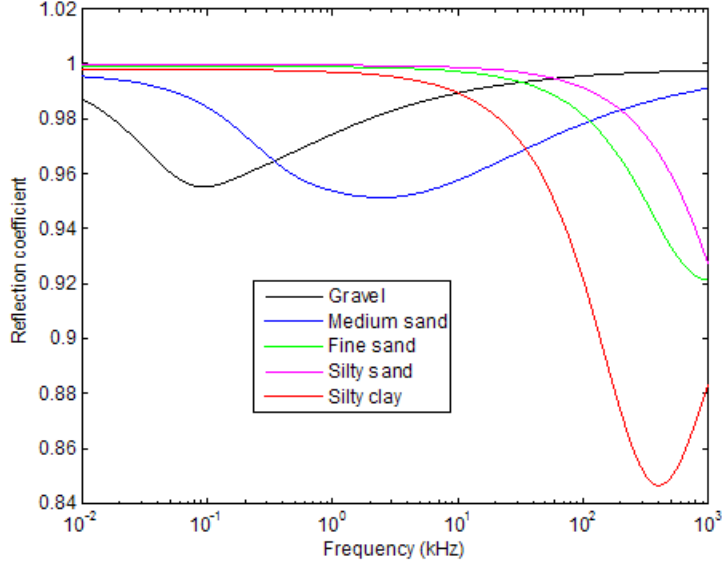
Figure 32: The reflection coefficient as a function of frequency at an incident angle of $5\,^\circ$. The sound speed in water was $1460\,\mathrm{m\,/\,s}$.

compressional wave speed and attenuation for the SAX99 sand.

An important aspect of SAX99 was that most of the parameters were measured sufficiently many times to permit estimation of parameter ranges. Figures 37 and 38 show the range of predictions that might result due to the parameter ranges given in Table 1. In particular if the parameter values were taken to be the midpoints of the ranges, the estimates of compressional wave speeds would be about 2% too high. In the worst case in which the data lay on the high curve of Figure 37, the midpoint values would have underestimated the wave speed by about 3.5%. On the other hand the predictions for wave attenuation would be about the same for any choice of values within the range.

5.2 The frame question

There are concerns about the Biot-Stoll model, insofar as its applicability to unconsolidated seabeds, centered around the extent to which an uncemented collection of grains, possibly not all of the same type of mineral, can be characterized as an elastic frame.

5.2.1 Is the model applicable to heterogeneous sediments?

The unjacketed test assumes that a single modulus K_r characterizes the frame material, which is clearly reasonable only for a homogeneous frame, that is,
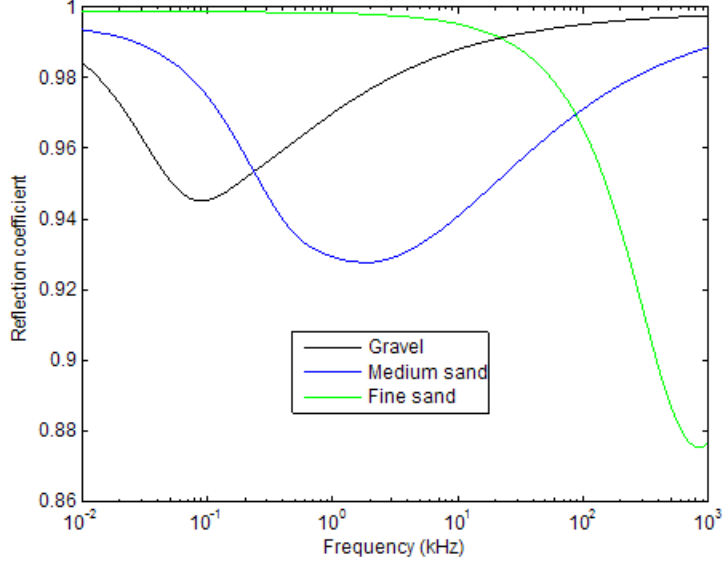
Figure 33: The reflection coefficient as a function of frequency at an incident angle of $5°$. The sound speed in water was $1530\,\mathrm{m\,/\,s}$.

one composed of grains of a single mineral. Biot and Willis [5] conjectured that a heterogeneous material might act as an "equivalent homogeneous solid", however Hickey and Sabatier [22] point out this would require that changes in grain shape due to deviatoric strains cancel out, which may be optimistic. Thus the question of what to do about heterogeneous materials remains open.

5.2.2 Is porosity constant?

Another question is whether in the unjacketed test porosity is unchanged when the specimen is subjected to fluid pressure. Quite possibly for an uncemented collection of grains it would change. In this case the moduli in (8) would be calculated using (9) rather than (11), but whereas the bulk modulus K_f of water is well known, it is not clear how to measure the modulus K_{fr}. Inversions on four data sets by Chotiros [16] gave values of K_{fr} that were $60\%, 62\%, 88\%, 61\%$ of the values K_{fr}^0 that would be obtained by use of (10). The 88% figure was from data on uncompacted laboratory sand. He calls the hypothesis $K_{fr} \neq K_{fr}^0$ the independent coefficient of fluid content hypothesis (ICFC). As is indicated in Figure 1, the Biot model prediction for compressional wave speed was higher than the measured values for the two measurements below one kHz. To see if the ICFC hypothesis might explain this let $K_{fr} = \theta K_{fr}^0$. Figures 39 and 40 show the results of varying θ on compressional wave speed and attenuation.
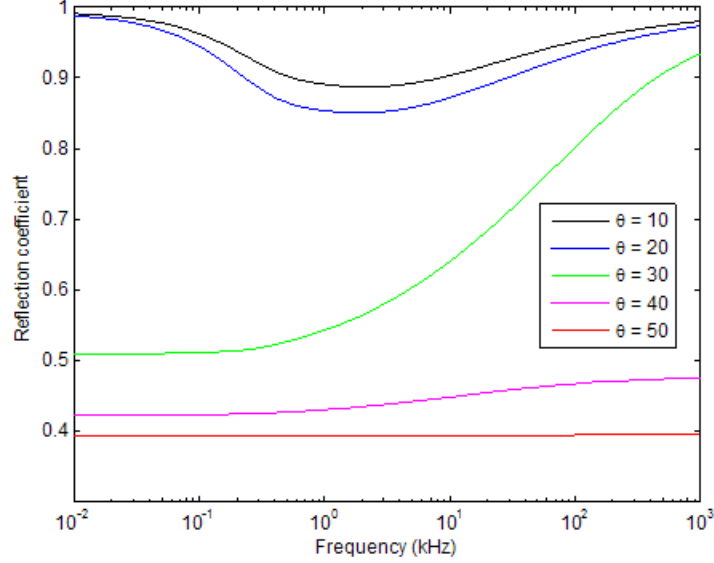
Figure 34: Reflection coefficient as a function of frequency for different incident angles for medium sand. The critical angle is around $30°$.

A value of around $\theta = 0.95$ sufficed to lower the low frequency predictions to near the measured values, but reduced the predictions at higher frequencies to well below the measured values. However as Figures 41 and 42 show this can be ameliorated by increasing the permeability from $k = 2.5 \times 10^{-11}\,\mathrm{m}^2$ to $k = 5 \times 10^{-11}\,\mathrm{m}^2$, and the tortuosity from $\alpha = 1.35$ to $\alpha = 1.12$ as was done to generate the "best fit" plot in Figure 1. Thus this hypothesis seems to have merit. It provides an alternative to simply raising the porosity to get a better fit to the low frequency data. On the other hand, while there is a hypothetical experiment by which the additional parameter K_{fr} might be measured in Biot and Willis [5], it is not clear whether it is practical. It should also be noted that the air bubble hypothesis of Chotiros and Isakson [17] (Section 3.3) leads to the same conclusion. Indeed if we accept (10), but use (41) to compute K_f, then the resulting value of D computed from (11) can be equated to that of (9), resulting in a one-to-one correspondence between the gas volume fraction and θ. Gas fractions of $\phi = 1, 3$ and 5 ppm correspond to values of $\theta = 0.984, 0.950$ and 0.919.

5.2.3 Should all of the grains be included in the frame?

A final difficulty with treating an unconsolidated sediment as an elastic frame is the problem of what should be included in the frame. In [28] it is shown that the
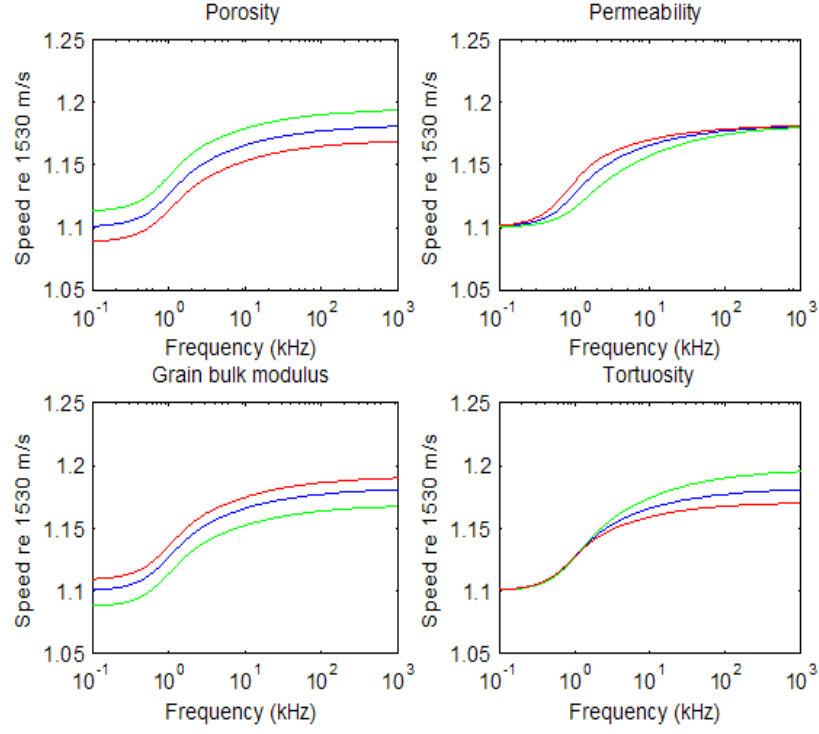
Figure 35: Influence of four Biot-Stoll parameters on compressional wave speed. The green curve used the lower bound for the parameter given in Table 1, Column 3, the red curve the upper bound, and the blue curve the midpoint. The midpoint values were used for all parameters other than the one being varied.
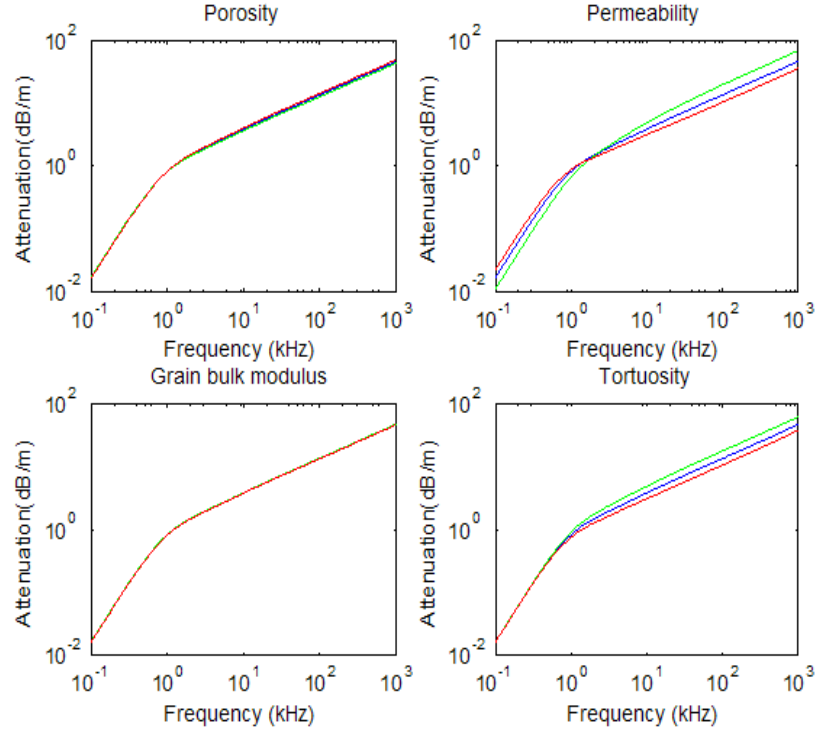
Figure 36: Influence of four Biot-Stoll parameters on compressional wave attenuation. The green curve used the lower bound for the parameter given in Table 1, Column 3, the red curve the upper bound, and the blue curve the midpoint. The midpoint values were used for all parameters other than the one being varied.
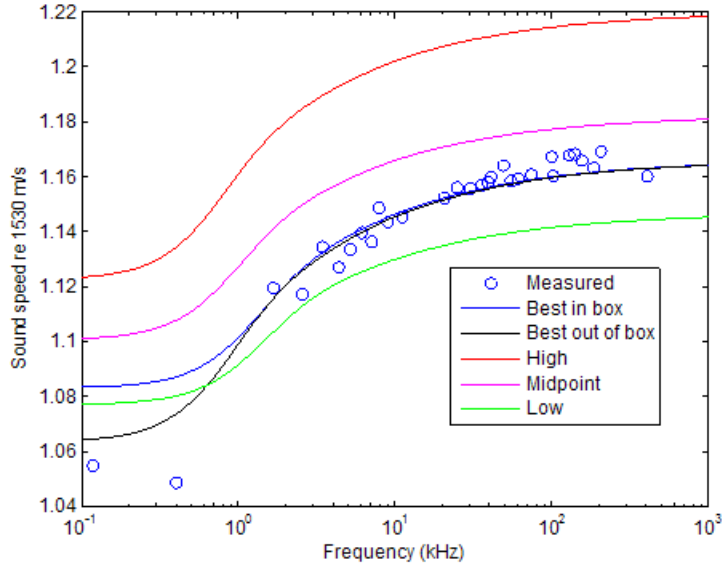
Figure 37: Range of predictions for compressional wave speed possible given the parameter ranges of Table 1, Column 3. The predictions labelled "Best in box" are those for the parameters of Column 4. The predictions labelled "Best out of box" are those of Column 4 with the changes $\beta = 41.5, \alpha = 1.12, k = 5 \times 10^{-11}$. The "Midpoint" curve used the midpoints of the ranges in Column 3. The "High" and "Low" curves were obtained by moving each the parameters porisity, permeablity, grain bulk modulus, and tortuosity to whichever range endpoint increased or decreased the wave speed respectively.
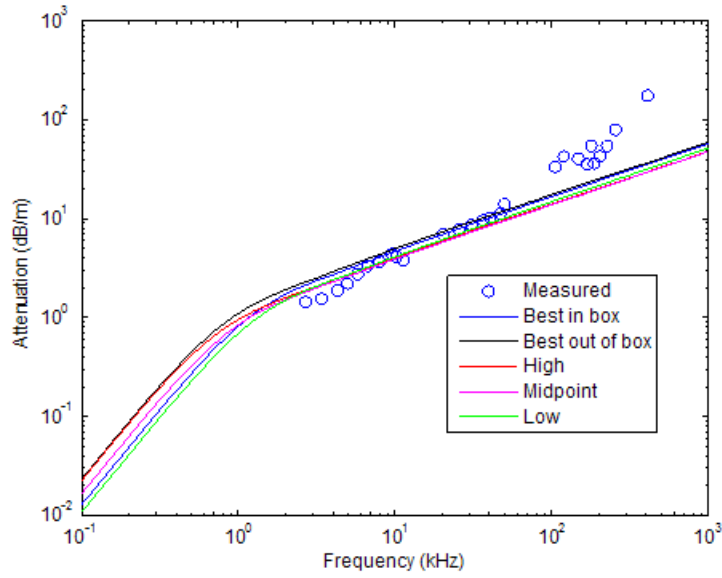
Figure 38: Range of predictions for compressional wave attenuation possible given the parameter ranges of Table 1, Column 3. The predictions labelled "Best in box" are those for the parameters of Column 4. The predictions labelled "Best out of box" are those of Column 4 with the changes $\beta = 41.5, \alpha = 1.12, k = 5 \times 10^{-11}$. The "Midpoint" curve used the midpoints of the ranges in Column 3. The "High" and "Low" curves were obtained by moving each the parameters porisity, permeablity, grain bulk modulus, and tortuosity to whichever range endpoint increased or decreased the wave speed respectively.
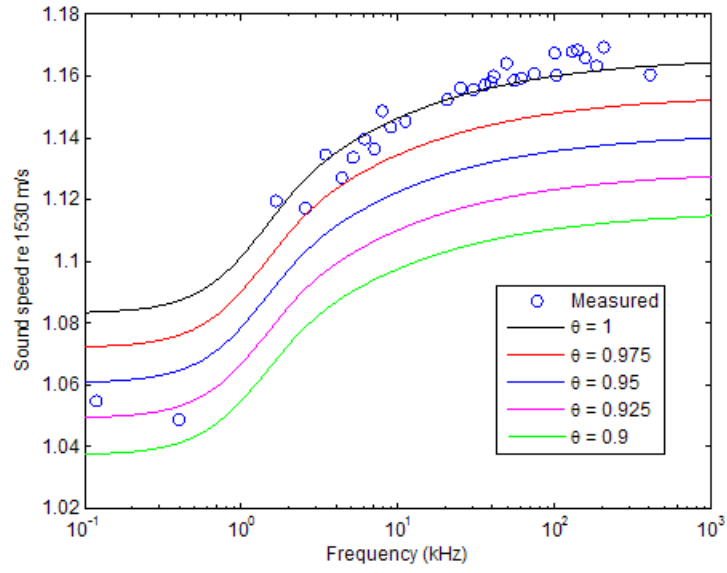
54

Figure 39: Result on compressional wave speed of varying the parameter θ in the equation $K_{fr} = \theta K_{fr}^0$.
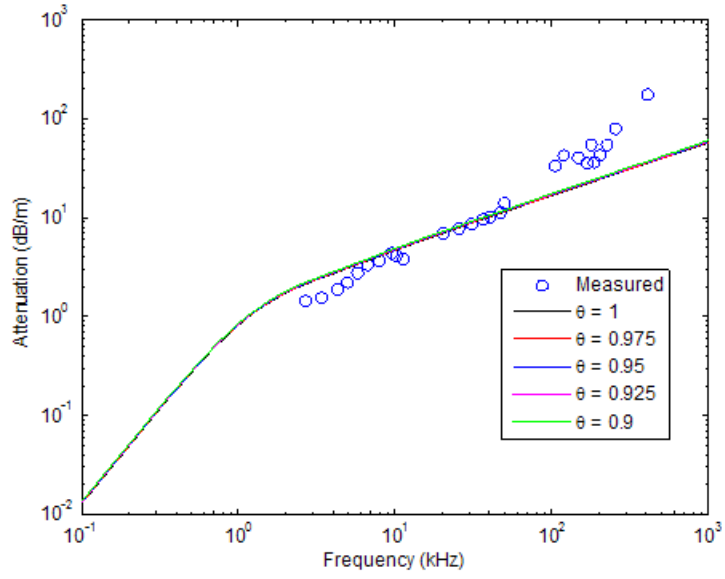
Figure 40: Result on compressional attenuation of varying the parameter θ in the equation $K_{fr} = \theta K_{fr}^0$.
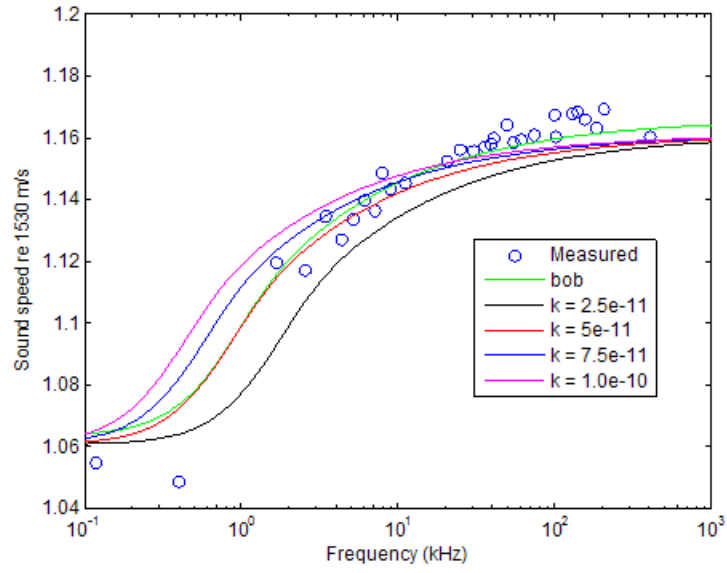
Figure 41: Result on compressional wave speed of varying permeability when $K_{fr} = \theta K_{fr}^0$ with $\theta = 0.95$. "bob" is the best fit from Figure 1.
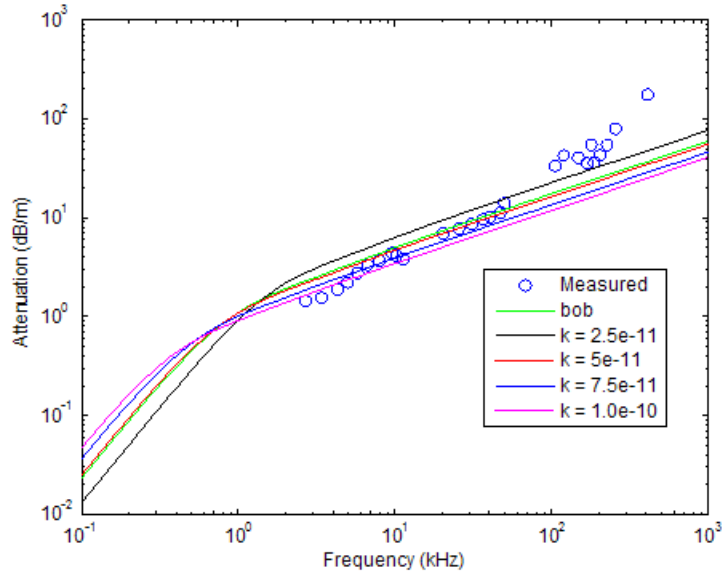
Figure 42: Result on compressional wave attenuation of varying permeability when $K_{fr} = \theta K_{fr}^0$ with $\theta = 0.95$. "bob" is the best fit from Figure 2.

application of an external force to a granular lattice causes the formation of force chains (see Figure 43). Thus it is not clear that all of the sedimentary grains should be considered part of the frame. Conversely it may be that some fluid is trapped in cracks in the grains or between grains and should be considered part of the frame. Chotiros [16] defined three additional porosities β_f, β_s and β_c. The first two are the portion of fluid trapped in the frame and the portion of the grains to be regarded as part of the fluid. The third, the composite porosity, is defined by

$$\beta_c = \frac{\beta - \beta_f}{1 - \beta_s - \beta_f}. \tag{59}$$

The composite densities and bulk moduli are defined to be

$$\rho_{rc} = (1 - \beta_f)\rho_r + \beta_f\rho_f, \rho_{fc} = (1 - \beta_s)\rho_f + \beta\rho_r \tag{60}$$

$$K_{rc} = \frac{K_r K_f}{(1 - \beta_f)K_f + \beta_f K_r}, K_{sc} = \frac{K_r K_f}{(1 - \beta_s)K_r + \beta_s K_f}.$$

Inversions on four data sets gave values of $\beta_f = 0.15, 0, 0, 0$ and $\beta_s = 0.36, 0.36, 0.07, 0.31$ for seabeds of porosity $\beta = 0.37, 0.36, 0.41, 0.40$ giving composite porosities $\beta_c = 0.44, 0.57, 0.44, 0.58$ which are considerably higher than the measured porosities. This hypothesis, which Chotiros calls the composite materials (CM) hypothesis, did not seem to explain the higher apparent porosity, $\beta = 0.415$, for the SAX99 data. However since the bulk moduli K_f and K_r occur only in the unjacketed test (see Section 2.1) where the presence or absence of force chains would be irrelevant, it is not clear that the use of the composite moduli $(60)_2$ is required. If one leaves K_f and K_r as they are and replaces all instances of β, ρ_f and ρ_r by their composites given in (59) and $(60)_1$, then the resulting predictions are shown in Figures 44 and 45. It should be noted that these graphs are sufficiently similar to those of Figures 39 and 40 that the composite materials and independent coefficient of fluid content hypotheses are indistinguishable on the basis of their predictions of wave speed and attenuation alone.

5.3 The "fast slow wave" controversy

When in three experiments waves having an apparent speed of about $1200\,\mathrm{m\,/\,s}$ were detected at subcritical grazing angles, Chotiros [15] conjectured that they were Type II compressional waves. As indicated in Figure 26 Type II waves are not predicted to have speeds nearly that large with the parameter values conventionally used in the Biot-Stoll model. To arrive at a Type II wave speed of 1200 m/s Chotiros suggested, based upon measurements of the grain bulk modulus by Molis and Chotiros [31], that the value of the grain bulk modulus K_r should be around $7 \times 10^9\,\mathrm{Pa}$ as opposed to the conventional value of about $4 \times 10^{10}\,\mathrm{Pa}$, which is the bulk modulus of quartz crystals[7]. As indicated in

---

[7]Chotiros suggests that the quartz crystal value is not applicable because of cracks and other imperfections in the sand grains.
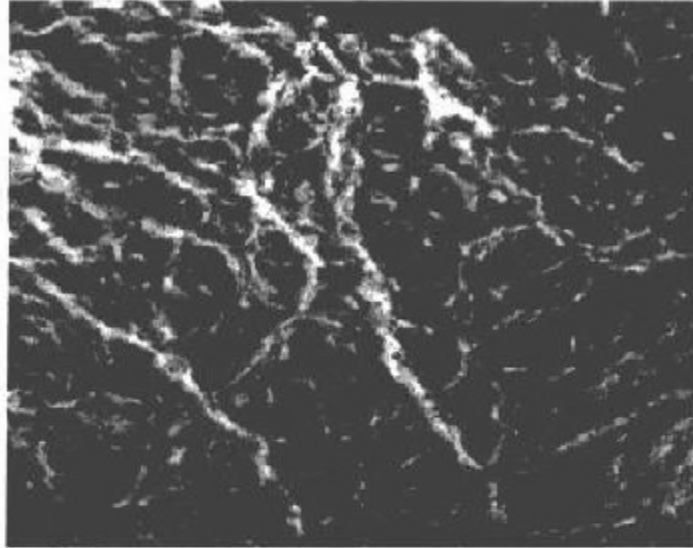
Fig. 1. An image of the force chains in a granular medium as viewed between two crossed circular polarizers. The particles, 3-mm Pyrex spheres, are surrounded by an index-matching fluid, a mixture of glycerol and water. The beads are placed in a box with sides 70 mm by 70 mm by 40 mm; the image size is 40 mm by 42 mm. A 200-N force is exerted on a piston that covers the top surface. The stressed beads can be seen as bright regions (the brightness is due to their stress-induced birefringence).

SCIENCE • VOL. 269 • 28 JULY 1995
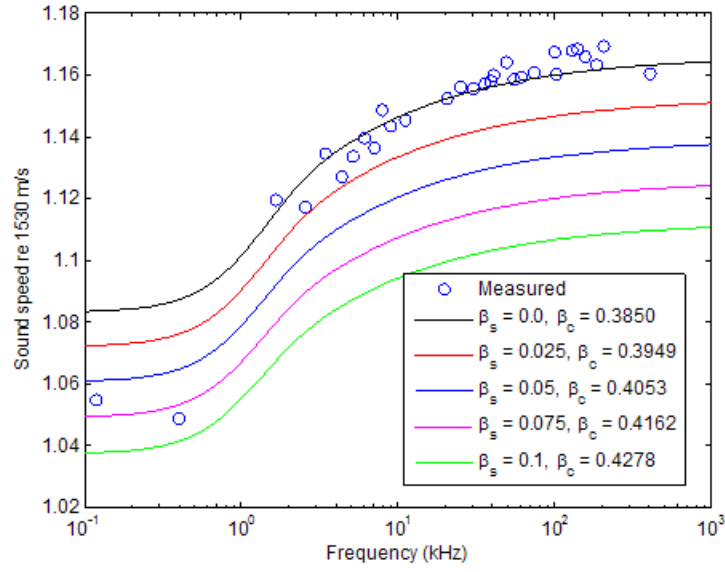
Figure 43: Illustration of a force chain in sand.

Figure 44: Compressional wave speeds for the SAX99 sand when the proportion β_s of grains to be included in the pore fluid is varied. The proportion β_f of fluid included in the frame was assumed to be zero. The parameters used were those of Table 1, Column 4.
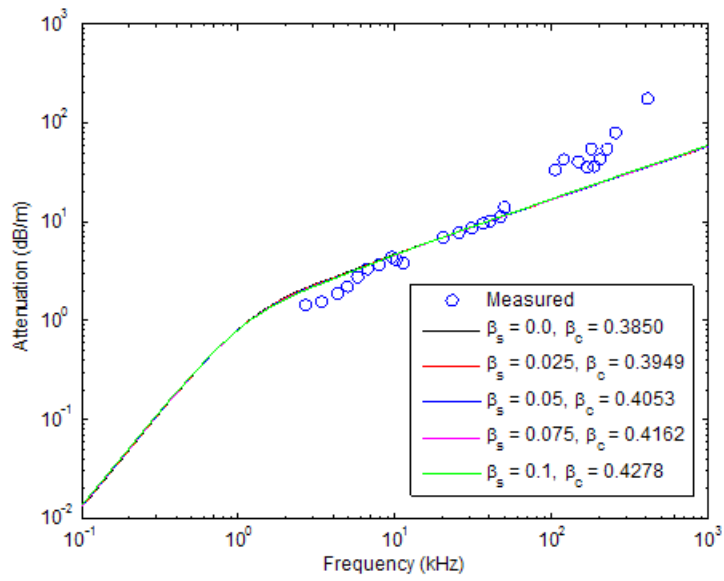
Figure 45: Compressional wave attenuation for the SAX99 sand when the proportion β_s of grains to be included in the pore fluid is varied. The proportion β_f of fluid included in the frame was assumed to be zero. The parameters used were those of Table 1, Column 4.
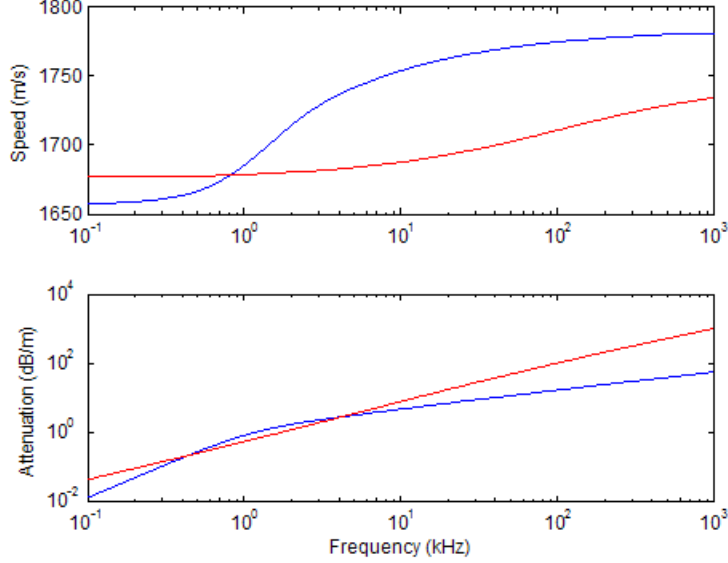
Figure 46: The effect of using the non-conventional parameter values $K_r = 7 \times 10^9$ Pa, Re $K_b = 5.3 \times 10^9$ Pa suggested by Chotiros on the predictions for Type I waves of the Biot model for the SAX99 sediment. Blue lines are the predictions for the SAX99 best fit parameters of Table 1. Red lines are the predictions resulting from the alternative parameters.

Figure 35, lowering the value of K_r lowers the predicted Type I wave speeds. To achieve agreement with the measured Type I wave speeds in the three experiments Chotiros assumed a frame bulk modulus of $K_b = 5.3 \times 10^9$ Pa, which is about 50 times larger than the conventional values. Figures 46 and 47 show the effects of these modifications on the predictions for the SAX99 sand. Type I compressional waves become less dispersive with respect to frequency and the growth of attenuation more nearly linear with respect to frequency. Type II waves now have speeds in the 1200-1400 m/s range at frequencies above 1 kHz and are less attenuated.

Subsequent work, both experimental and theoretical, has tended to refute Chotiros' conjecture. As indicated above the SAX99 measurements confirmed the conventional values (Table 1). Simpson and Houston [35] found in laboratory experiments that for a smoothed water-sediment interface no waves other than those having the expected speeds of Type I waves could be detected, but for a roughened interface and shallow grazing angles a wave with an apparent speed of 1200 m/s was detected. The authors state "However, for near normal incidence, these measurements have enough temporal resolution to clearly show that this later time arrival is better described by the roughened interface scattering, which
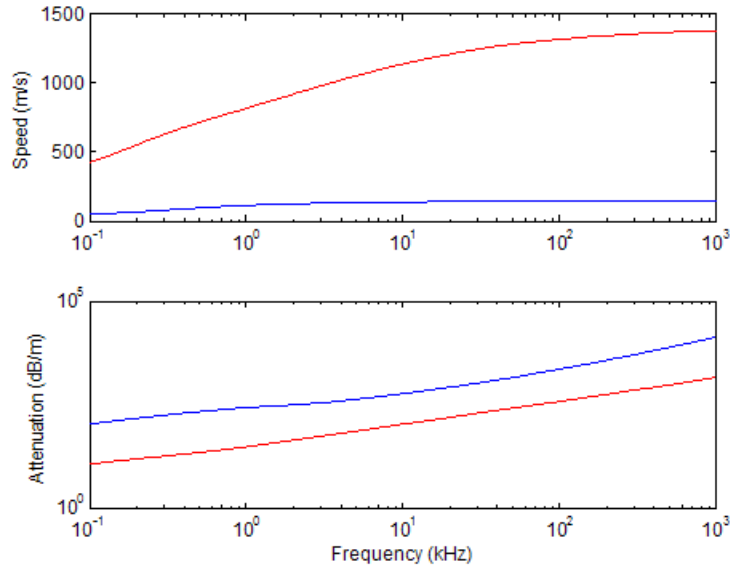
Figure 47: The effect of using the non-conventional parameter values $K_r = 7 \times 10^9$ Pa, $\mathrm{Re}\, K_b = 5.3 \times 10^9$ Pa suggsted by Chotiros on the predictions for Type II waves of the Biot model for the SAX99 sediment. Blue lines are the predictions for the SAX99 best fit parameters of Table 1. Red lines are the predictions resulting from the alternative parameters.

give the appearance of a wave front with a virtual wave speed of 1200 m/s at shallow ensonification angles, rather than by a 1200 m/s slow compressional wave." On the theoretical side Hickey and Sabatier [22] argue on the basis of the Voigt-Reuss-Hill formulae that for the mineral composition of the sand used in one of Chotiros' experiments the grain bulk modulus must lie between 3.3×10^{10} and 3.7×10^{10} Pa. This range does not encompass Chotiros' value of $K_r = 7 \times 10^9$ Pa. They also argue that the constraint

$$\beta < 1 - K_b/K_r < 1$$

([5]) requires that $K_b < 4.2 \times 10^9$ Pa which again is not consistent with Chotiros' value of $K_b = 5.3 \times 10^9$ Pa.

5.4   The Biot model's predictions

5.4.1   The controversy about the growth of attenuation with increasing frequency

It is generally agreed that internal dissipation generates wave attenuation that is linear in frequency [26]. The Biot model's prediction that compressional wave attenuation is not necessarily a linear function of frequency, but is more like f^2 at low frequencies and $f^{1/2}$ at high frequencies is due to viscous losses. This prediction has been a source of controversy for nearly three decades. Hamilton [21] stated "The number studies of attenuation in sands from 1-100 kHz affirm an approximate first-power relationship between attenuation and frequency, and deny any $f^{1/2}$ relationship as called for by Stoll in this frequency range." More recently Buckingham [11] asserted "A substantial body of data supports the view that compressional-wave attenuation in many porous, granular materials varies more or less accurately as the first power of frequency, f^1, over an extended frequency range, from 1 Hz up to 1 MHz." On the other hand Kibblewhite stated in a survey article [26] "... in spite of the sparsity of data for marine sediments at low frequencies, the widely held assumption that the relationship between attenuation and frequency is linear from seismic to ultrasonic frequencies does not appear justified." Brunson and Johnson [9] measured shear wave attenuation in the 1-10 kHz range and found "... for a sediment of this type, the relative motion of the pore fluid, and the sediment skeletal frame is a significant contributor to the observed loss of energy...". Turgut and Yamamoto [43] found that "Consistency between predicted and directly measured porosity and permeability indicates that the viscous loss mechanism has a major effect on attenuation in the frequency range of 1-30 kHz for sandy sediments." The source of the difficulty is illustrated in Figure 2. It not easy to differentiate between the predictions of the Biot and Buckingham model in the frequency range 1-100 kHz, and this historically has been the range in which most measurements of attenuation have been made. The SAX99 measurements do seem to indicate that the Biot model's prediction of attenuation varying as $f^{1/2}$ at high frequencies is wrong, and this is progress.

As pointed out in [44] experimental evidence for strong velocity dispersion, as predicted by the Biot model, is also evidence that attenuation cannot be a linear function of frequency. Causality dictates the Kramers-Kronig integral relations between wave speed and attenuation. In O'Donnel *et al.* [32] it is argued that the Kramers-Kronig integral relations lead to the following approximate local relation between wave speed c and attenuation α (in nepers/m)

$$\frac{dc(\omega)}{d\omega} = \frac{2}{\pi\omega^2} c(\omega)^2 \alpha(\omega). \tag{61}$$

Thus for the Buckingham model which predicts, to the first order in ω, that attenuation is given by $\alpha = \gamma\omega$, wave speeds must be logarithmically dispersive

$$c = \left(-\frac{2\gamma}{\pi} \ln \omega + K \right)^{-1}.$$

Figure 48 shows the Kramers-Kronig compatible fit to the SAX99 data from [44]

$$c = \left(\frac{1}{c_1} - \frac{2\gamma}{\pi} \ln \left(\frac{\omega}{\omega_1} \right) + i\gamma + \frac{s_0}{1 - i\tau\omega} \right)^{-1} \tag{62}$$

with $c_1 = 1705\,\text{m/s}, \omega_1/2\pi = 100\,\text{Hz}, \gamma = 5.50 \times 10^{-6}\,\text{Np}\cdot\text{s/m}, \tau = 0.3\,\text{ms}, s_0 = 0.05\,\text{ms/m}$, as well as the prediction of the Buckingham model. As can be seen Kramers-Kronig relation implies that a strong velocity dispersion necessitates a departure from attenuation that is linear in frequency. There is other evidence for strong velocity dispersion. Maguer *et al.* [30] have found that experiments on subcritical penetration of energy into the seabed suggest a substantially lower compressional speed than is measured from cores at $200\,\text{kHz}$ and that these lower speeds are compatible with those predicted by the Biot model. Turgut and Yamamoto [43] also found velocity dispersion compatible with Biot model predictions in cross-hole tomography experiments (see Figure 53). Thus while the SAX99 data tends to affirm f^1 growth at high frequencies, it adds to the evidence that low frequency attenuation is not proportional to f^1.

6 Incorporation of frequency-dependent viscoelastic mechanisms

As indicated in Figures 1 and 2 the "standard" Biot model with frequency-independent bulk and shear moduli fails to agree with the SAX99 data in two significant ways. It predicts wave speeds that were higher than measured at low frequencies, at least if the parameters are confined to the ranges given in Table 1, Column 3., and it predicts attenuations that are too low at high frequencies. Ways of addressing the low frequency problem have been addressed above. One can posit air bubbles in the pore space as Chotiros and Isakson did in [17] (Sections 2.4,3.3). Alternatively one can adopt the independent coefficient of fluid content (ICFC) hypothesis discussed in Section 5.2.2 or the composite
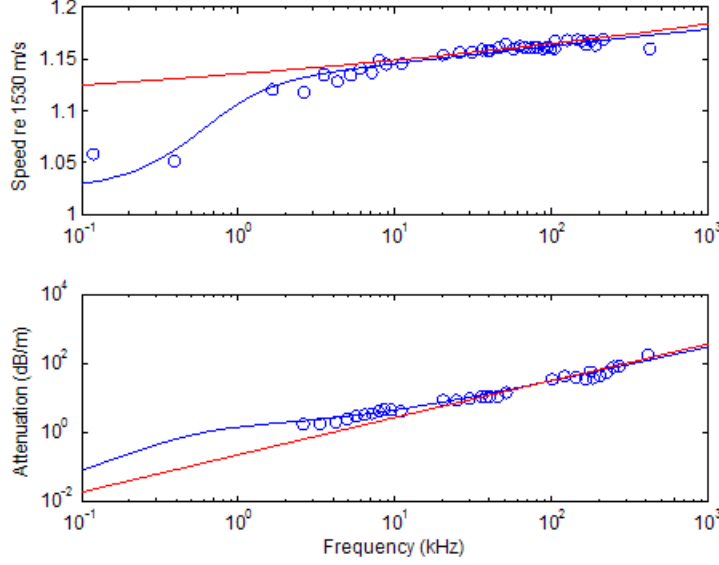
Figure 48: Blue line: Kramers-Kronig compatible fit to SAX99 compressional wave and attenuation data. Red line: Predictions of the Buckingham model.

material (CM) hypothesis of Section 5.2.3. As can be seen in Figures 44 and 39 any of these conjectured mechanisms have the effect of simply translating the wave speed curves downward and thus, absent any means of determining the controlling parameters other than choosing them to agree with the measured data, there is no way to distinguish among them. The problem of the poor predictions for attenuation at high frequencies has been addressed recently by means of the BICSQS model discussed in Section 2.4. In this section we examine the extent to which it rectifies this problem.

As a starting point we took the midpoints of the intervals in Table 1, Column 3 as the values of the Biot-Stoll parameter (see Figure 37). The Poisson ratio, which has negligible effect, was set to $\nu = 0.15$, following [17]. The shear modulus was adjusted to give the experimentally measured value of 120 m/s [44]. The Reuss model of composite compressibility (41) was used to obtain agreement with the low frequency wave speed data by specifying a gas volume fraction ϕ. Agreement with the high frequency measurements for wave speed and attenuation were obtained by manipulating the parameters K_y and f_μ respectively. Finally agreement with the measured values of wave speed and attenuation in the $1 - 10$ kHz range was obtained, to the extent possible, by adjusting the bulk relaxation frequency f_k. A compromise was required here because values that improved agreement with attenuation worsened it with respect to wave speed. Figures 49 and 50 show the results of these machinations

Parameter	Units	SAX-CI	SAX-Mid/Dps	TY
Porosity β		0.37	0.3785	0.44
Grain density ρ_r	kg/m^3	2690	2690	2650
Fluid density ρ_f	kg/m^3	1023	1023	1000
Grain bulk modulus K_r	GPa	36	40.5	36
Effective fluid bulk modulus K_f	GPa	2.15	2.19	2.25
Fluid viscosity η	kg/m-s	0.001	0.00105	0.001
Permeability k	μ^2	115	33	17.5
Pore size a	μ	57	31	28
Structure factor α		1.35	1.38	1.24
Frame shear modulus μ	GPa	0.028	0.03	0.024
Gap modulus K_y	GPa	0.968	0.8/0.9	0.9
Bulk relaxation frequency f_k	kHz	4.8	4/1.5	3.2
Shear relaxation frequency f_μ	kHz	56	70/80	10^6
Gas fraction ϕ	$\times 10^{-6}$	6.7*	5.5	1.4*
Pore size std dev σ		0	0/1.25	0

Table 6: SAX-CI: Parameters for the SAX99 sediment used by Chotiros and Isakson. SAX-Mid: Midponits of the parameter ranges in Column 3 of Table 1. The alternative Dps values in Column 4 assume distributed pore sizes. TY: The parameters Chotiros and Isakson used to model the cross-hole tomography experiemnt of Tugut and Yamamto. The parameters marked with * were calculated using the Reuss model for composite compressibilities. Chotiros and Isakson used a different model. The TY data was not measured at sufficiently high frequencies to ascertain the shear relaxation frequency. Chotiros and Isakson listed it as "infinity".

along with the curves that Chotiros and Isakson arrived at by using the same procedure. The fit that Chotiros and Isakson arrived at is somewhat better, but as indicated in Table 6, they used a value of permeability that was more than three times the midpoint of the estimated range given in Table 1. The only rationale they give for this adjustment is that "This is consistent with observations that permeability measurements may only be accurate to within an order of magnitude." As pointed out in Section 3.4 permeability was measured in three different ways during the SAX99 exercise and none of them arrived at a value nearly as high as the Chotiros-Isakson value. This being the case, a better alternative may be to use the distributed pore size viscosity correction factor of Yamamoto and Turgut [45] presented in Section 2.5.2. Figures 51 and 52 show that when a standard deviation of $\sigma = 1.25$ is assumed and the mean pore size distribution is computed from (39) and the midpoint of the permeability range in Table 1, agreement with the SAX99 data is comparable to that obtained by Chotiros and Isakson.

In [17] Chotiros and Isakson discuss the predictions of their BICSQS model for five sets of data taken from the literature. Other than the SAX99 data
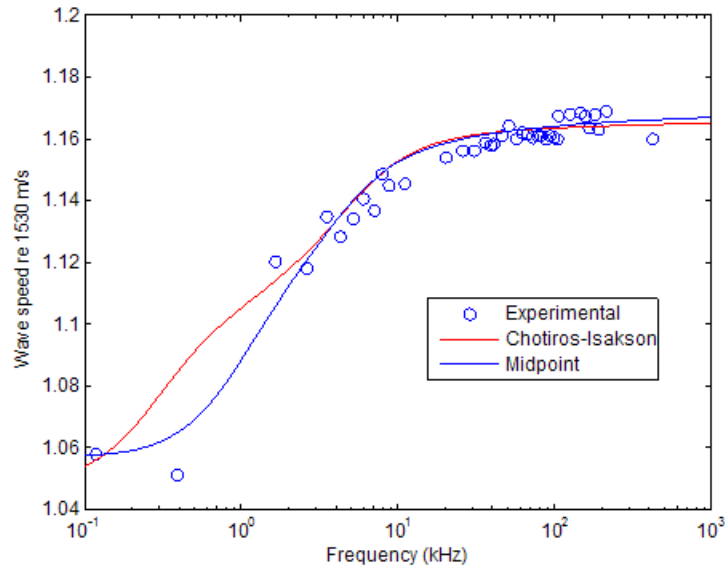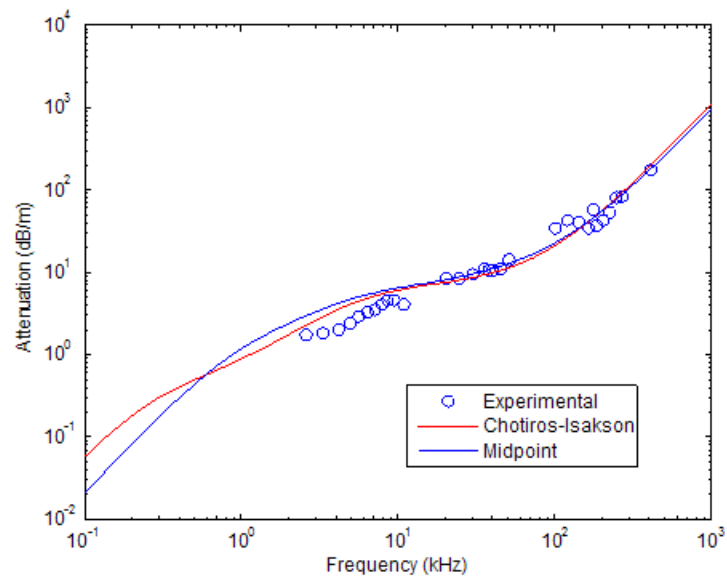
Figure 49: Best fits to SAX99 wave speed data.

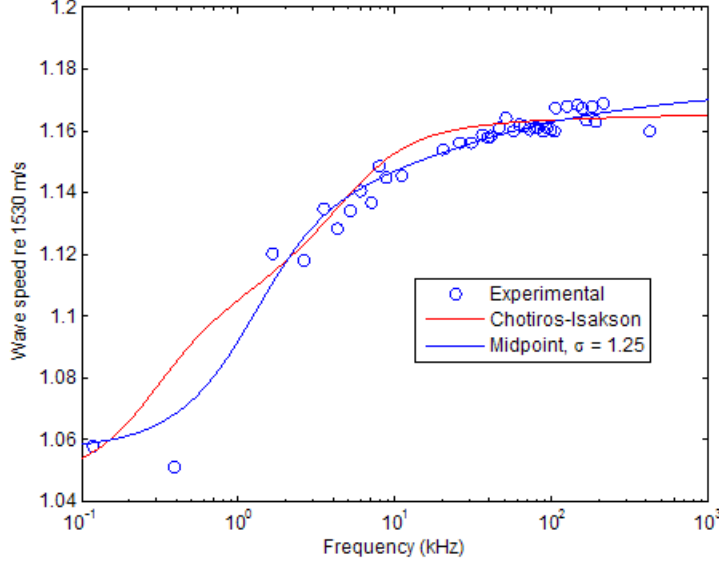Figure 50: Best fit to the SAX99 attenuation data.

Figure 51: Best fit to the SAX99 wave speed data, assuming distributed pore sizes.

the only one of the five that has measurements of compressional wave speed against frequency are the cross-hole tomography experiments of Turgut and Yamamoto [43]. Figures 53 and 54 show Chotiros and Isakson's best fit to the wave and attenuation data. Table 6, Col. 5 gives the parameters they used.

It may be noted that the experimental values of wave speed in Figure 53 ascend with frequency more quickly than is predicted by the BICSQS model. Figure 55 shows that a better fit to the wave speed data can be obtained by incorporating Biot's model for air bubble resonance (equation (30)) discussed in Section 2.4. Figure 56 shows that with or without bubble resonance the BICSQS model overestimated the compressional wave attenuation in the lower frequency range. However Turgut and Yamamoto ([43], Figure 6) indicate that calculating the wave speeds from the measured attenuation using the approximate local Kramers-Kronig relations (61) somewhat underestimated the measured wave speeds. This is illustrated in Figure 57 where it is seen that the wave speeds computed from (61) using numerical integration on the attenuation data in Figure 56 are not in as good agreement with the measured wave speed values as the wave speeds calculated from (61) using the higher attenuation values predicted by the four-mode bubble resonance model.
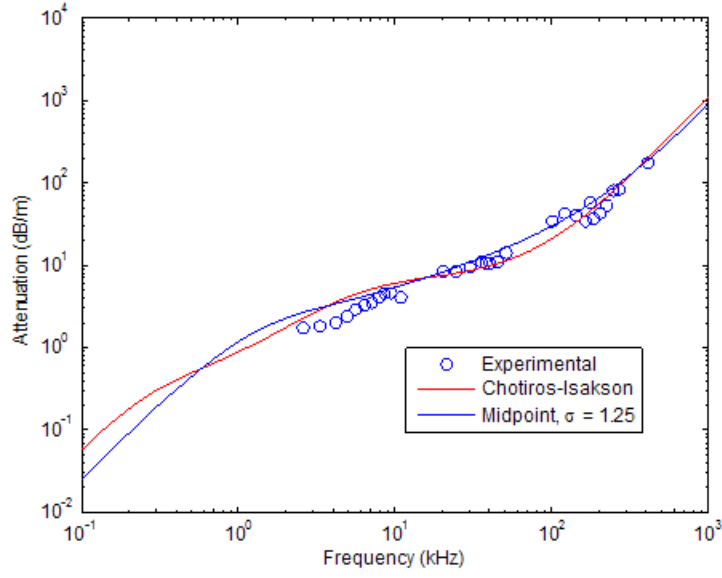
Figure 52: Best fit to the SAX99 attenuation data, assuming distributed pore sizes.

Parameter	Units	CI	Bubble resonance
Gap modulus K_y	GPa	1.35	0.55
Bulk relaxation frequency f_k	kHz	4.75	3.2
Shear relaxation frequency f_μ	kHz	10^6	100
Gas fraction ϕ	$\times 10^{-6}$	3.75	3.75
Pore size std dev σ		0	0
Resonant frequency f_a	kHz		4.5
Damping parameter b_a	MPa-s		0.7

Table 7: Parameters used to compare the BICSQS model with (Col. 4) and without (Col 3) air bubble resonance. The TY data was not measured at sufficiently high frequencies to ascertain the shear relaxation frequency. Chotiros and Isakson listed it as "infinity".
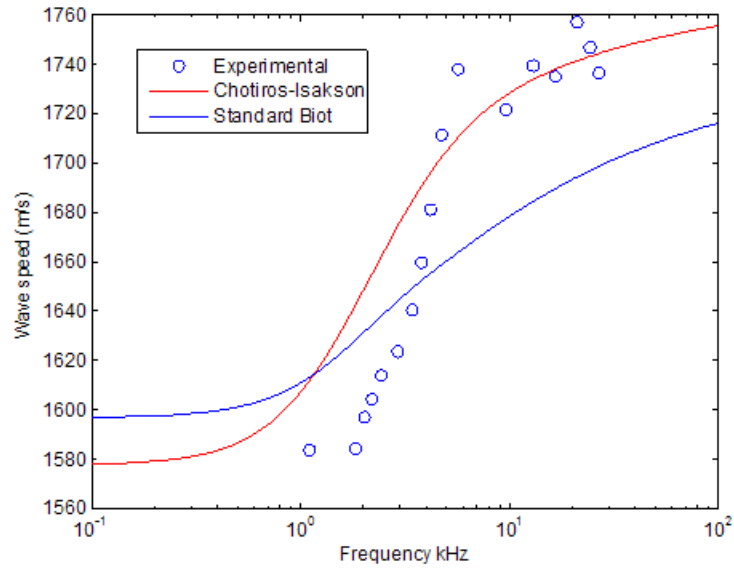
71

Figure 53: Best fit, as determined by Chotiros and Isakson [17], to wave speed data of the cross-hole tomography of Turgut and Yamamoto [43]. Also shown are the predictions of the standard Biot model with $K_b^* = 43.6 + 2.08i$ MPa, $\mu^* = 29.2 + 1.8i$ MPa .
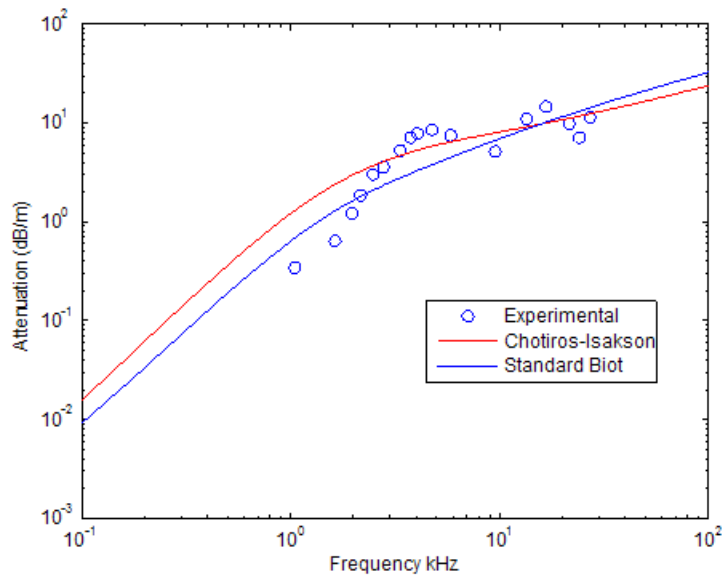
Figure 54: Best fit, as determined by Chotiros and Isakson [17], to wave attenuation data of the cross-hole tomography of Turgut and Yamamoto [43]. Also shown are the predictions of the standard Biot model with $K_b^* = 43.6 + 2.08i\,\mathrm{MPa}, \mu^* = 29.2 + 1.8i\,\mathrm{MPa}$.
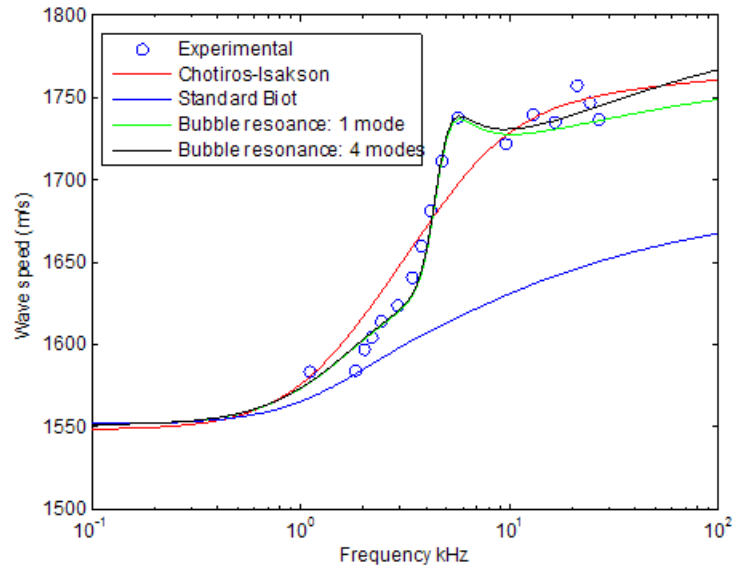
Figure 55: The predictions of the BICSQS model when air bubble resonance is included. The parameters used are given in Table 7. The curve labeled Chotiros-Isakson was obtained by reducing the effective fluid bulk modulus to agree with the value which gave good agreement at low frequencies in the bubble resonant case and the adjusting the gap modulus and bulk relaxation frequencies to improve the fit. "Modes" refers to the number of modes used in equation (28).
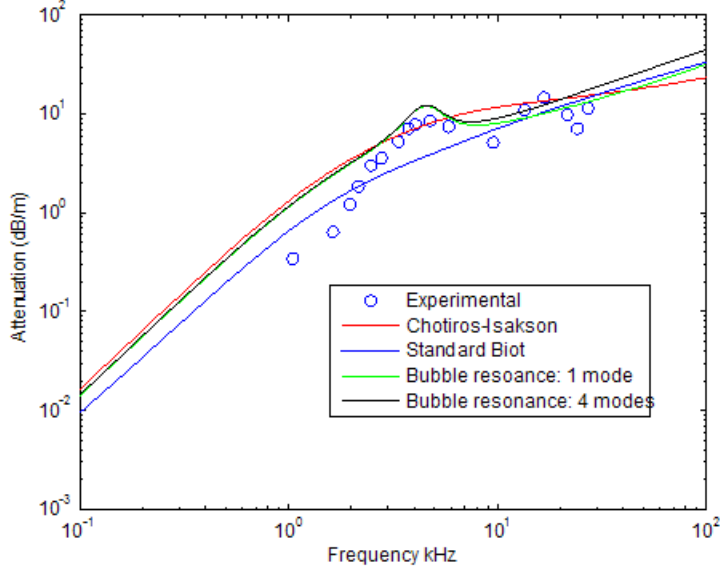
Figure 56: See Figure 55 for a description of the models being compared.

7 Summary and Conclusions

One long-standing objection to the Biot model is that its predictions for compressional wave attenuation are not in accord with a substantial body of experimental evidence that attenuation in unconsolidated sediments grows linearly with frequency. The measurements made in the SAX99 exercise confirmed this approximately linear relation, at least at frequencies above 10 kHz. The use of frequency-dependent moduli suggested by Chotiros and Isakson [17] (but also by Biot [8]) in lieu of the frequency-independent moduli traditionally used, seems to adequately address this problem.

There are two reasons to challenge the Biot model on theoretical grounds. One is the objection of Hickey and Sabatier [22] that the Biot model is not applicable to heterogeneous sediments (Section 5.2.1). This criticism is valid, but it is unknown what effect this deficiency has on the predictions of the model. The other criticism of the model is the assumption that an unconsolidated sediment can be modelled as a Hookean elastic solid of constant porosity which encompasses all of the sand grains. As discussed in Sections 5.2.2 and 5.2.3 this provides a feasible explanation of the poor agreement of the Biot model with low frequency data in the SAX99 exercise, at least when the measured parameter values are used. It should be noted however that the presence of air bubbles in the pore space provides an alternative explanation of these results, one which admits the possibility of air bubble resonance which might be of some utility
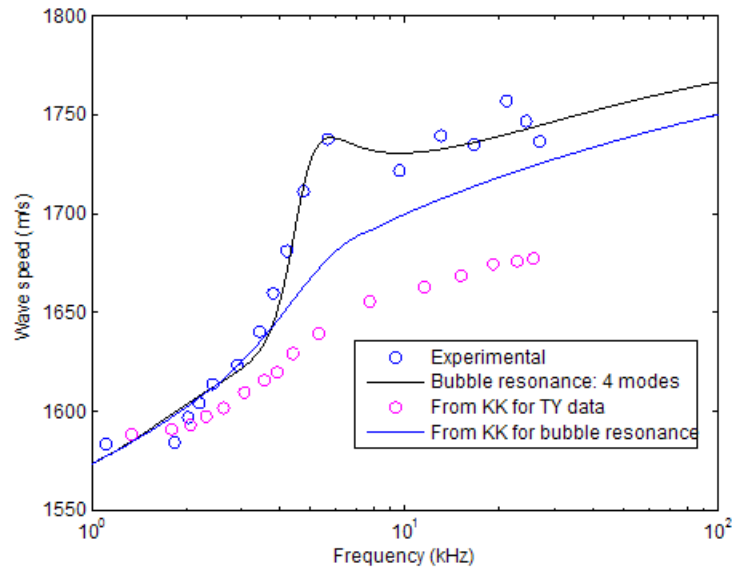
Figure 57: Comparison of the wave speeds predicted by the four-mode bubble-resonant BICSQS model with those calculated from the Kramers-Kronig relations. See the text for further explanation.

in explaining the results of the cross-hole tomography experiment of Turgut and Yamamoto [43] discussed in Section 6. As noted above, however, all of the postulated mechanisms make predictions too similar to distinguish among them.

The major concern about the Biot model that remains is its complexity and the number of parameters that are important, but difficult, or at least expensive to measure. The BICSQS model of Chotiros and Isakson does not (disregarding the uninfluential introduction of the Poisson ratio) increase the number of parameters in the model, however it does replace four parameters $\mathrm{Re}\,K_b^*, \mathrm{Im}\,K_b^*, \mathrm{Re}\,\mu^*, \mathrm{Im}\,\mu^*$, none of which have much influence on compressional wave speed and attenuation, with three parameters, the gap modulus K_y and the relaxtaion frequencies f_k and f_μ all of which strongly influence the BICSQS model's predictions in certain frequency ranges. We currently have no means of determining these parameters other than from measured values of wave speed and attenuation in the appropriate frequency range. Likewise the distributed pore size version of Biot's viscosity correction factor due to Yamamoto and Turgut [45] should be used in lieu of Biot's original, since there is every reason to believe that pore size distribution is not uniform. This again replaces a relatively uninfluential parameter in the standard Biot model, pore size, with the standard deviation parameter σ_ϕ, which as indicated in Figure 14, can have a substantial effect on the Biot model's predictions, at least if $\sigma_\phi \approx 1$ or 2 as is conjectured.

In summary, with the enhancements suggested by Chotiros and Isakson and Yamamoto and Turgut, the Biot model is now robust enough to explain all extant measurements of compressional wave speed and attenuation using plausible physical mechanisms. Its predictive value is still in question because of the difficulty of determining the parameters upon which it depends.

References

[1] M. Badiey, A. Cheng, and Y. Mu. From geology to geoacoustics - evaluation of the Biot-Stoll sound speed and attenuation for shallow water acoustics. *J. Acoust. Soc. Am.*, 103(1):309–320, 1998.

[2] J.H. Beebe, S.T. McDaniel, and L.A. Rubano. Shallow-water transmission loss prediction using the Biot sediment model. *J. Acoust. Soc. Am.*, 71(6):1417–1426, 1982.

[3] M. A. Biot. General theory of three-dimensional consolidation. *J. Applied Physics*, 12(2):155–164, February 1941.

[4] M. A. Biot. Mechanics of deformation and acoustic propagation in porous media. *J. Applied Physics*, 33(4):1482–1498, April 1962.

[5] M. A. Biot and D. G. Willis. The elastic coefficients of the theory of consolidation. *J. Appl. Mech.*, 24:594–601, 1957.

[6] M.A. Biot. Theory of propogation of elastic waves in a fluid-saturated porous solid. I. Lower frequency range. *J. Acoust. Soc Am.*, 28(2):168–178, 1956.

[7] M.A. Biot. Theory of propogation of elastic waves in a fluid-saturated porous solid. II. Higher frequency range. *J. Acoust. Soc. Am.*, 28(2):179–191, 1956.

[8] M.A. Biot. Generalized theory of acoustic propagation in porous dissapative media. *J. Acoust. Soc. Am.*, 34(5):1254–1264, September 1962.

[9] B.A. Brunson and R.K. Johnson. Laboratory measuements of shear wave attenuation in saturated sand. *J. Acoust. Soc. Am.*, 68(5):1371–1375, 1980.

[10] G.M. Bryan and R.D. Stoll. The dynamic shear modulus of marine sediments. *J. Acoust. Soc. Am.*, 83:2159–2164, 1988.

[11] M. J. Buckingham. Theory of acoustic attenuation, dispersion, and pulse propagation in unconsolidated granular materials including marine sediments. *J. Acoust. Soc. Am.*, 102(5):2579–2596, 1997.

[12] M. J. Buckingham. Theory of compressional and shear waves in fluidlike marine sediments. *J. Acoust. Soc. Am.*, 103(1):288–299, 1998.

[13] M. J. Buckingham. Wave propagation, stress relaxation, and grain-to-grain shearing in saturated unconsolidated sediments. *J. Acoust. Soc. Am.*, 108(6):2796–2815, 2000.

[14] R. Burridge and J.B. Keller. Poroelasticity equations derived from microstructure. *J. Acoust. Soc. Am.*, 70:1140–1146, 1981.

[15] N.P. Chotiros. Biot model of sound propagation in water-saturated sand. *J. Acoust. Soc. Am.*, 97(1):199–214, 1995.

[16] N.P. Chotiros. An inversion for Biot parameters in water-saturated sands. *J. Acoust. Soc. Am.*, 112(5):1853–1868, 2002.

[17] N.P. Chotiros and M.J. Isakson. A broadband model of sandy ocean sediments: Biot-Stoll with contact squirt flow and shear drag. *J. Acoust. Soc. Am.*, 116(4):2011–2022, 2004.

[18] J. Dvorkin and A. Nur. Dynamic poroelasticity: A unified model with the squirt and the Biot mechanisms. *Geophysics*, 58(4):524–533, 1993.

[19] J. Gittus. *Creep, Viscoelasticity and Creep Fracture in Solids.* John Wiley and Sons, New York, 1975.

[20] T.J. Haire and C.M. Langton. Biot theory: A review of its application to ultrasound propagation through cancellous bone. *Bone*, 24(4):291–295, 1999.

[21] E.L. Hamilton. Geoacoustic modeling of the seafloor. *J. Acoust. Soc. Am.*, 68(5):1313–1340, 1980.

[22] C.J. Hickey and J.M. Sabatier. Choosing Biot parameters for modeling water-saturated sands. *J. Acoust. Soc. Am.*, 102(3):1480–1484, 1997.

[23] C. W. Holland and B. A. Brunson. The Biot-Stoll model: An experimental assessment. *J. Acoust. Soc. Am.*, 84(4):1437–1443, 1988.

[24] J.M. Hovem and G.D. Ingram. Viscous attenuation of sound in saturated sand. *J. Acoust. Soc. Am.*, 66(6):1807–1812, 1979.

[25] D.L. Johnson, J. Koplik, and R. Dashen. Theory of dynamic permeability and tortuosity in fluid-saturated porous media. *J. Fluid Mech.*, 176:379–402, 1987.

[26] A.C. Kibblewhite. Attenuation of sound in marine sediments: A review with emphasis on new low frequency data. *J. Acoust. Soc. Am.*, 86(2):716–738, 1989.

[27] W.C. Krumbein and G.D. Monk. Permeability as a function of the size parameters of unconsolidated sand. *Petr. Technol. Am. Inst Mining Metall. Eng.*, 1492:1–9, 1942.

[28] C.h. Liu, S.R. Nagel, D.A. Schecter, S.N. Coppersmith, S. Majumdar, O. Narayan, and T.A. Witten. Force fluctuations in bead packs. *Science*, 269:513–515, 1995.

[29] A. E. H. Love. *A Treatise on the Mathematical Theory of Elasticity.* Dover, New York, fourth edition, 1944.

[30] A. Maguer, E. Bovio, W.L.J. Fox, and H. Schmidt. In situ estimation of sediment sound speed and critcal angle. *J. Acoust. Soc. Am.*, 108(3):987–996, 2000.

[31] J.C. Molis and N.P. Chotiros. A measurement of grain bulk modulus of sands. *J. Acoust. Soc. Am.*, 91:2463(A), 1992.

[32] M. O'Donnel, E.T. Jaynes, and J.G. Miller. Kramers-Kronig relationship between ultrasonic attenuation and phase velocity. *J. Acoust. Soc. Am.*, 69(3):696–701, 1981.

[33] M.D. Richardson, K.B. Briggs, L.D. Bibee, P.A.Jumars, W.B. Sawyer, D.B. Albert, R.H. Bennet, T.K. Berger, M.J. Buckingham, N.P. Chotiros, P.H. Dahl, N.T. Dewitt, P. Fleischer, R. Flood, C.F. Greenlaw, D.V. Holliday, M.H. Hulbert, M.P. Hutnak, P.D. Jackson, J.S. Jaffe, H.P. Johnson, D.L. Lavoie, A.P. Lyons, C.S. Martens, D.E. McGehee, K.D. Moore, T.H. Orsi J.N. Piper, R.I. Ray, A.H. Reed, R.F. Liko Self, J.L. Schmidt, S.G. Schock, F. Simonet aand R.D Stoll, D. Tang, D.E. Thistle, E.I. Thorsos, D.J. Walter, and R.A. Wheatcroft. An overview of SAX99: Environmental considerations. *IEEE J. Oceanic Eng.*, 26(1):26–53, 2001.

[34] M.D. Richardson, E. Muzi, B. Miaschi, and F. Turgutcan. Shear wave velocity gradients in near-surface marine sediment. In J.M. Hovem, M.D. Richardson, and R.D. Stoll, editors, *Shear Waves in Marine Sediments*, pages 295–304. Kluwer Academic Publishers, 1991.

[35] H.J. Simpson and B.H. Houston. Synthetic array measurements of acoustical waves propagating into a water-saturated sandy bottom for a smoothed and roughened interface. *J. Acoust. Soc. Am.*, 107(5):2329–2337, 2000.

[36] M. Stern, A. Bedford, and H.R. Milwater. Wave reflection from a sediment layer with depth-varying properties. *J. Acoust. Soc. Am.*, 77(5):1781–1788, 1985.

[37] R.D. Stoll. Acoustic waves in saturated sediments. In L. Hampton, editor, *Physics of Sound in Marine Sediments.*, pages 19–39. Plenum, 1974.

[38] R.D. Stoll. *Sediment Acoustics*, volume 26 of *Lecture Notes in Earth Sciences*. Springer-Verlag, 1989.

[39] R.D. Stoll and G.M. Bryan. Wave attenuation in saturated sediments. *J. Acoust. Soc. Am.*, 47(5 (Part 2)):1440–1447, 1970.

[40] R.D. Stoll and T.-K. Kan. Reflection of acoustic waves at a water sediment interface. *J. Acoust. Soc. Am.*, 70(1):149–156, 1981.

[41] E.I. Thorsos, K.L. Williams, N.P. Chotiros, J.T. Christoff, K.W. Commander, C.F. Greenlaw, D.V. Holliday, D.R Jackson, J.L. Lopes, D.E. Magehee, J.E. Piper, M.D. Richardson, and D. Tang. An overview of SAX99: Acoustic measurements. *IEEE J. Oceanic Eng.*, 26(1):4–25, 2001.

[42] A. Turgut. An investigation of causality for Biot models by using Kramers-Kronig relations. In J.M. Hovem, M.D. Richardson, and R.D. Stoll, editors, *Shear Waves in Marine Sediments*, pages 403–410. Kluwer Academic Publishers, 1991.

[43] A. Turgut and T. Yamamoto. Measurements of acoustic wave velocities and attenuation in marine sediments. *J. Acoust. Soc. Am.*, 87(6):2376–2383, 1990.

[44] K.L. Williams, D.R. Jackson, E.I. Thorsos, D. Tang, and S.G. Schock. Comparison of sound speed and attenuation measured in a sandy sediment to predictions based on the Biot theory of porous media. *IEEE J. Oceanic Eng.*, 27(3):413–428, 2002.

[45] T. Yamamoto and A. Turgut. Acoustic wave propagation through porous media with arbitrary pore size distributions. *J. Acoust. Soc. Am.*, 83(5):1744–1751, 1988.